Journal of Structural Dynamics, 1, (pp. 1-29) 2021
Damping of coupled bending-torsion beam vibrations by a two-dof tmd with analogous coupling

Journal of Structural Dynamics

Damping of coupled bending-torsion beam vibrations by a two-dof tmd with analogous coupling

Jan Høgsberg *[1]

[1] *Department of Mechanical Engineering, Technical University of Denmark, Nils Koppels Allé, building 404, DK-2800 Kongens Lyngby, Denmark*

Abstract

Coupled bending-torsion vibrations of a beam with a single cross-section axis of symmetry are mitigated by a two-degree-of-freedom (dof) tuned mass damper with a coupling analogous to that of the beam. By modal truncation a four-degree-of-freedom model is derived for tmd tuning. Because of the analogous tmd properties, a stiffness tuning formula identical to that for the classic tuned mass damper secures inverse relations between all four undamped natural frequencies. Expressions for the tmd damping are subsequently found by a numerical search, which maximizes the smallest of the four damping ratios, resulting in equal damping in three of the four modes. The two-dof coupled tmd is finally assessed by numerical root locus and frequency response analysis for a full flexible beam.

Keywords: Structural dynamics; Coupled vibrations; Damping; Tuned mass damper

Received on January 5, 2021, Accepted on June 23, 2021, Published on July 1, 2021

1 Introduction

Beam models are effectively used to describe the dynamics of slender structural elements, such as bridges, blades or wings. Most of these structural elements have cross-sectional geometries without axes of symmetry, whereby inherent coupling between transverse bending and torsion occurs due to non-coinciding centroid (mass midpoint) and shear center. Figure 1(a) illustrates this inertial bending-torsion coupling for a non-symmetric blade section. The blade is assumed to accelerate transversely with a, resulting in an opposite inertia force $P \propto a$ at the cross-section centroid C (cross). Because of the centroid's eccentricity e to the shear center O (dot), the inertia force P will as well impose the torsional moment $M_x = eP$ shown in Fig. 1(b), which creates a twist in the blade, illustrating the vibrational bending-torsion coupling to be accounted for in the present paper when designing a two-degree-of-freedom (two-dof) tuned mass damper (tmd) with analogous coupling properties.

Various theories have been applied to specifically describe the vibrational bending-torsion coupling effect for beams with non-symmetric cross-sections, for example concerning vibrations of wind turbines blades [1], the dynamics of bridge decks excited by moving loads (train passage) [2, 3] or flutter [4] and saw tooth blade vibrations [5]. The original theoretical basis for the vibrations of beams with fully non-symmetric cross-sections is presented by Gere and Lin [6] and references therein. Several contributions to the development and solution of coupled beam equations have since been published, of which only a few are reviewed here. When using separation of variables with assumed temporal harmonic motion, the spatial solution is governed by a polynomial equation in a wavenumber-type variable. Initially, Friberg [7] considers beam vibrations for a fully non-symmetric cross-section, without lines of symmetry, thus governed only by a 5th-order polynomial equation in the wavenumber as the torsional stiffness contribution from in-plane warping is omitted.

* jhg@mek.dtu.dk

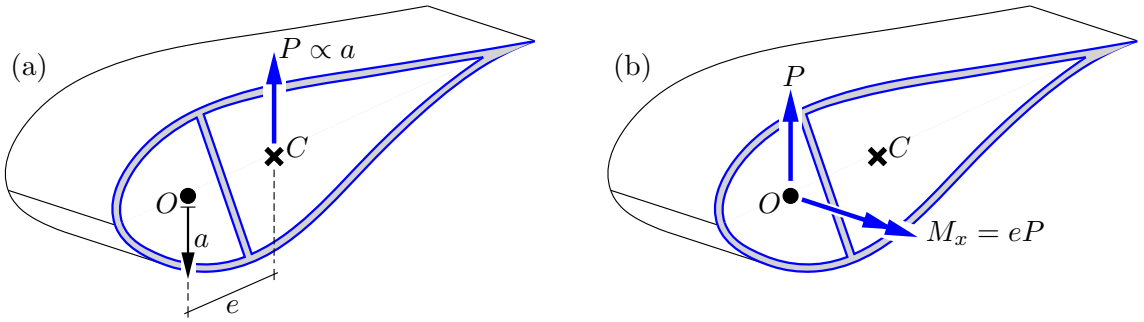

Fig. 1: (a) Wind turbine blade with transverse load P in mass midpoint C from assumed downward acceleration a. (b) Eccentricity e to shear center O implies a torsional moment $M_x = eP$ that illustrates the inertial bending-torsion coupling for beams with non-symmetric cross-sections.

For the simpler single-symmetric cross-section, torsion only couples with a single transverse direction. This problem is addressed by both Dokumaci [8] and Banerjee [9] in its purest form, without shear flexibility, cross-sectional rotary inertia and in-plane warping, thus enabling the determination of real-valued spatial solutions based on trigonometric and hyperbolic functions. This simple double-coupled vibration problem governs the dynamic properties of the host structure in Section 2 of the present paper, to which an analogously double-coupled two-degree-of-freedom (two-dof) tmd is attached in the subsequent Section 3. The simplest double-coupling problem in [8, 9] has been further extended by accounting for additional effects, such as warping stiffness in Bishop et al. [10], shear flexibility and cross-section rotary (Timoshenko beam) by Banerjee and Williams [11] and most recently combined warping stiffness and rotary inertia, see Ambrosini et al. [12].

The original triple-coupling problem [7] has been extended by Bercin and Tanaka [13] and by Arpaci and Bozdag [14], in both cases with the addition of warping stiffness, whereby their characteristic equations become of 6th polynomial order. The addition of cross-section rotary inertia is subsequently addressed by Arpaci et al. [15], while comparison with experimental natural frequencies is furthermore presented in Ambrosini [16]. Some modifications of the above mentioned beam vibration problems have as well been considered, such as the coupling of torsion with a pure shear transverse element [17] or the recent inclusion of beam tapering [18, 19]. Also different solution methods have been proposed, with the usage of beam finite elements (FE) by assumed spatial interpolation with cubic polynomials as the most common approach, see e.g. Mei [20] or Tanaka and Bercin [21] for some of the more general applications of FE.

The present papers specifically considers damping and mitigation of the resonant double-coupled bending-torsion beam vibrations in [8, 9]. For resonant vibration problems, the so-called tuned mass dampers (or vibration absorbers) are particularly effective, as they synchronize an auxiliary inertia to a specific vibration frequency, to which all damping effort can then be focused. The classic tmd, with a single-directional mass suspended by a parallel spring-dashpot element, is proposed by Brock [22] and Den Hartog [23]. An initial summary of explicit design expressions for the classic tmd is provided by Warburton [24] for various loading and optimization conditions. The equivalence between pole placement and response mitigation (H_∞) is demonstrated by Krenk [25], who furthermore proposes a slightly larger damping coefficient to minimize tmd deflections. Tmd tuning that accounts for structural damping has been a longstanding issue, as it complicates otherwise simple calibration expressions. A review is provided by Asami et al. [26], who also propose simplified expressions for the tmd parameters when accounting for structural damping.

Recently, a two-terminal tuned inerter damper (tid) has been proposed for damping of structures by Lazar et al. [27] or simply as a supplement to the auxiliary tmd mass in [28, 29]. In particular for pure inerter-based absorbers, the influence or spill-over from non-resonant structural vibration modes may deteriorate the accuracy of the underlying tuning methods, which might therefore require some compensation, e.g. by the artificial stiffness and inertia terms proposed in [30]. A recent review of vibration control by tmds is provided by Elias and Matsagar [31].

When a classic tmd (or tid) is installed to target a specific structural vibration mode, the frequency response curve will exhibit two distinct peaks around the original resonance frequency, which for optimal damper tuning will become practically flat. When adding additional tmds, these can be jointly optimized to further lower (and also widen) the resonance peak region, as demonstrated by Ma et al. [32] for up to a three-dof tmd, thereby creating a flat plateau by balancing four closely spaced resonance peaks with sufficient amount of damping. This design procedure can be extended to even more tmd-dofs, as argued and numerically demonstrated by da Costa et al. [33].

A two-dof tmd (the simplest multi-dof tmd) has recently been proposed and investigated by installing an inerter inside the tmd's spring-dashpot element, see e.g. [34, 35, 36], which also creates a reduction in response amplitude

by three well-balanced peaks. The addition of an inerter element is also found to improve energy harvesting from ambient vibrations [37]. A two-dof tmd can as well be applied to mitigate two vibration modes, as shown for the symmetric cruciform absorber proposed by Snowdon et al. [38], while reduction of three resonance peaks requires a three-dof tmd, see Jang and Choi [39]. By Meng et al. [40] it was furthermore concluded that two two-dof tmds perform slightly better than four classic tmds, illustrated for the four dominant vibration modes of a long-span bridge model. Equivalent two-dof tmd (or tid) systems can alternatively be realized by shunted piezoelectric devices, either placed within a mechanical tmd [41] or independently by a double-inductive LRLC shunt [42].

The desired coupling in multi-dof-tmds has mostly been implemented by assuming non-identical stiffness and damping in two parallel spring-dashpot elements, supporting an auxilliary mass that can as well rotate. However, in [43, 44, 45, 46] these notoriously coupled tmds are merely designed and tuned to act as plain two-dof tmds on a pure single-dof structure model, thereby aiming at a three-peak flat plateau for a single resonance in the frequency response curve. However, an inherently coupled two- or three-dof tmd may be effective in damping of the previously described (double or triple) bending-torsion coupled vibrations for beams with non-symmetric cross-sections. The present paper thus addresses the design and tuning of a two-dof coupled tmd for damping and mitigation of the double-coupled bending-torsion beam vibrations in [8, 9]. Recently, Hoffmeyer and Høgsberg [47] have demonstrated how a set of three classic tmds can be balanced to operate effectively on a single vibration mode for a triple-coupled beam, for which the inherent coupling with the two other coupled modes may strongly disturb the tmd's performance.

In the present paper, a coupled two-dof tmd is designed and tuned to simultaneously target both vibration forms associated with a double-coupled bending-torsion beam mode. The two-dof tmd is deliberately constructed to have the same inertia coupling as the beam model, with the same apparent distance e between centroid and its (shear) center between the two identical spring-dashpot elements. It is demonstrated that when the coupling of the tmd dofs is chosen to exactly replicate the underlying bending-torsion beam coupling, the tmd stiffness can be explicitly calibrated based on inverse point properties for the four and two natural frequencies associated with vanishing and infinite tmd damping, respectively. A detailed description of how inverse point relations can be used in absorber tuning is found in [25, 41, 48]. The applied analogous principle, assuming similarity between structure and absorber, has recently been used in damping of e.g. nonlinear structures by a piezoelectric absorber with an analogous type of nonlinearity [49] and plate vibrations by a spatially analogous distribution of shunted piezoelectric laminates [50]. These examples suggest that complex structural vibrations can be effectively mitigated by an analogous vibration absorber system that accurately mirrors the governing vibration properties of the host structure.

In Section 2 the governing coupled beam equations are presented and reduced to a two-dof structure model by modal truncation. An analogous two-dof tmd is then attached to the host structure model in Section 3, hereby constituting a resulting four-degree-of-freedom (four-dof) system. In Section 4 the tmd stiffness is initially calibrated to obtain inverse point properties for all real-valued system roots, while explicit expressions for the damping parameter are subsequently determined by a numerical search. Finally, the performance of the analogously coupled two-dof tmd is demonstrated for a fully flexible beam in Section 5, assessed in terms of both root-locus diagrams and frequency response curves.

2 Coupled two-dof structural model

Coupled bending-torsion vibrations of beams occur for cross-sections with only a single (or no) axis of symmetry. A coupled two-degree-of-freedom (two-dof) model is obtained by modal truncation in the associated partial differential equations. In the subsequent Section 3, a two-dof tuned mass damper (tmd) is then designed with coupling properties analogous to those of the structural model.

2.1 Beam model

For beams with only a single axis of symmetry, vibrations will – because of the non-coinciding centroid and shear center locations – inherently experience bending-torsion vibrational coupling, as illustrated in connection with Fig. 1. Gere and Lin [6] summarized a detailed mathematical formulation for the coupled vibration problem, which in the following is used to establish a simplified two-dof structural model for a beam with a single axis of symmetry [8, 9].

2.1.1 Equations of motion

Consider a beam with longitudinal coordinate x, as illustrated in Fig. 2. The transverse deflection of the shear centre is described by the dependent variable $v(x,t)$, while $\theta(x,t)$ represents the beam's angle of twist. The beam is assumed

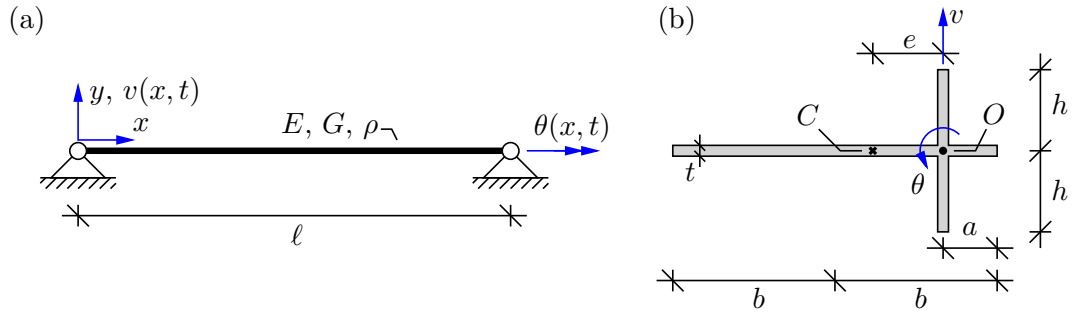

Fig. 2: (a) Beam with single-symmetric cruciform cross-section in (b). Non-vanishing distance e between shear center O (dot) and centroid C (cross) implies bending-torsion coupling in (1).

homogeneous with non-varying cross-sectional parameters. Thus, according to [6, 8, 9], the coupled partial differential equations

$$\rho A\ddot{v}(x,t) - \rho Ae\ddot{\theta}(x,t) + EIv(x,t)'''' = p(x,t) \tag{1}$$
$$\rho I_O\ddot{\theta}(x,t) - \rho Ae\ddot{v}(x,t) - GK\theta(x,t)'' = r(x,t) \tag{2}$$

govern the beam's dynamic properties with $\dot{(\,)} = \partial(\,)/\partial t$ and $(\,)' = \partial(\,)/\partial x$ representing partial temporal and spatial derivatives, respectively. In the beam equations, EI is the bending stiffness associated with the cross-section centroid C in Fig. 2(b), GK is the stiffness associated with pure st. Venant torsion, ρ is the material density, A is the cross-section area, I_O is the polar moment of inertia relative to the shear center O in Fig. 2(b), while e is the distance from the shear center O to the centroid C, as depicted for the blade in Fig. 1(a) and in Fig. 2(b) for a cruciform cross-section. The subsequent design and calibration of the coupled tmd omits the external loading from a distributed transverse force $p(x,t)$ and torsional moment $r(x,t)$. It follows from the second term on the left hand side of each equation (1) and (2) that the beam vibrations decouple for double symmetric cross-sections with $e = 0$. To retain the simplest possible mathematical model, equation (2) omits any stiffness contributions from in-plane warping associated with inhomogeneous Vlasov-type torsion.

2.1.2 Modal representation and equations

Without external loading, i.e. $p(x,t) = 0$ and $r(x,t) = 0$, and with specific homogeneous boundary conditions, the equations (1) and (2) constitute an eigenvalue problem, governing the natural frequencies and vibration modes for the coupled bending-torsion vibrations. A solution may be obtained by assuming the modal representations

$$v(x,t) = \sum_j^\infty X_j(x)u_j(t) \qquad , \qquad \theta(x,t) = \sum_k^\infty Y_k(x)\varphi_k(t) \tag{3}$$

with expansion functions $X_j(x)$ and $Y_k(x)$ representing the eigenfunctions from the uncoupled eigenvalue problems associated with $e = 0$ in both (1) and (2).

The modal representations in (3) are substituted into (1) and (2), which are then multiplied with $X_s(x)$ and $Y_s(x)$, respectively, and finally integrated over the length of the beam ℓ. The last term in each of these equations is then integrated by parts until the order of differentiation is the same in both expansion functions, whereby the associated boundary terms will cancel because of the boundary conditions. The two ordinary differential equations obtained for a coupled mode $j = k = s$ can then be written as

$$\rho A\int_0^\ell X_s(x)X_s(x)dx\,\ddot{u}_s(t) - \rho Ae\int_0^\ell X_s(x)Y_s(x)dx\,\ddot{\varphi}_s(t) + EI\int_0^\ell X_s(x)''X_s(x)''dx\,u_s(t) \simeq 0 \tag{4}$$
$$\rho I_O\int_0^\ell Y_s(x)Y_s(x)dx\,\ddot{\varphi}_s(t) - \rho Ae\int_0^\ell X_s(x)Y_s(x)dx\,\ddot{u}_s(t) + GK\int_0^\ell Y_s(x)'Y_s(x)'dx\,\varphi_s(t) \simeq 0 \tag{5}$$

where the approximate signs account for the truncation of any coupling terms without orthogonality between $X_j(x)$ and $Y_k(x)$ for $j \neq k$. In the following tmd calibration analysis, '$\simeq$' is simply replaced by '=', while the replacement is exact in the numerical example in Section 5 with sinusoidal expansion functions.

2.1.3 Two-dof structure model

The ordinary differential equations (4) and (5) constitute the coupled two-dof structural model illustrated in Fig. 3, with translation $u_s(t)$ and rotation $\varphi_s(t)$ at the shear center (dot) located at distance e_s relative to the centroid (cross). In this two-dof model, the shear center represents the midpoint between two translational springs with stiffness $\frac{1}{2}k_s$, while the centroid denotes the mass-midpoint of the lumped structural mass m_s. The rotational inertia of the lumped mass is j_s with respect to the mass midpoint (cross), whereby $J_s = j_s + e_s^2 m_s$ is the corresponding rotational inertia with respect to the model shear center (dot).

The coupled equations of motion for the two-dof mechanical model in Fig. 3 can be established from energy principles [6] or direct force equilibrium. They are conveniently written in symmetric form with respect to u_s and φ_s as

$$m_s\ddot{u}_s(t) + k_s u_s(t) - m_s\varepsilon_s a_s\ddot{\varphi}_s(t) = 0 \tag{6}$$

$$a_s^2(n_s + \varepsilon_s^2 m_s)\ddot{\varphi}_s(t) + k_s a_s^2\varphi_s(t) - m_s\varepsilon_s a_s\ddot{u}_s(t) = 0 \tag{7}$$

which introduces the relative eccentricity

$$\varepsilon_s = \frac{e_s}{a_s} \tag{8}$$

and the normalized rotational inertia

$$n_s = \frac{j_s}{a_s^2} \tag{9}$$

with respect to the cross-section centroid (cross).

Comparison of equations (4) and (5) with equations (6) and (7) directly identifies the relation between the mechanical two-dof model parameters and those of the modal beam model. The transverse mass m_s and stiffness k_s are directly obtained by comparison of the terms proportional to $\ddot{u}_s$ and u_s in (4) and (6), respectively:

$$m_s = \rho A\int_0^\ell X_s(x)X_s(x)dx \quad , \quad k_s = EI\int_0^\ell X_s(x)''X_s(x)''dx \tag{10}$$

The distance a_s is then governed by the rotational stiffness, obtained by comparison of the φ_s-terms in (5) and (7):

$$a_s^2 = \frac{GK\displaystyle\int_0^\ell Y_s(x)'Y_s(x)'dx}{EI\displaystyle\int_0^\ell X_s(x)''X_s(x)''dx} \tag{11}$$

The eccentricity is now obtained by comparing the coupling terms in either (4) and (6) or (5) and (7), which both give

$$\varepsilon_s = \frac{e}{a_s}\frac{\displaystyle\int_0^\ell X_s(x)Y_s(x)dx}{\displaystyle\int_0^\ell X_s(x)X_s(x)dx} \tag{12}$$

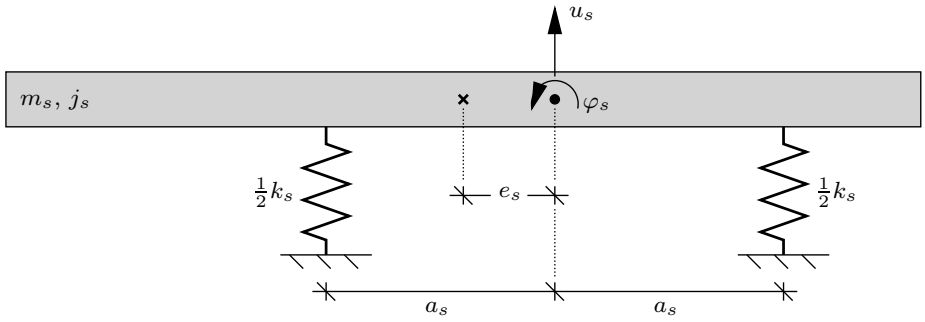

Fig. 3: Coupled two-degree-of-freedom (two-dof) structural model with equivalent properties determined by direct comparison with the modal equations in (4) and (5).

with a_s defined in (11). For identical expansion functions ($Y_s = X_s$) the relative eccentricity $\varepsilon_s = e/a_s$, in which case (8) gives $e_s = e$. Finally, the normalized rotational inertia is obtained by comparison of the $\ddot{\varphi}_s$-terms in (5) and (7):

$$n_s = \frac{\rho I_O}{a_s^2} \int_0^\ell Y_s(x)Y_s(x)dx - \rho A \varepsilon_s^2 \int_0^\ell X_s(x)X_s(x)dx \tag{13}$$

As n_s must be non-negative, it is found by (13) that the eccentricity e cannot exceed the cross-section's polar radius of inertia.

2.2 Eigenvalue analysis

When assuming complex harmonic solutions with angular frequency ω, the governing eigenvalue problem for free vibrations of the two-dof structural model can be readily obtained from (6) and (7) as

$$\left(\begin{bmatrix} k_s & 0 \\ 0 & k_s \end{bmatrix} - \omega^2 \begin{bmatrix} m_s & -m_s\varepsilon_s \\ -m_s\varepsilon_s & n_s + \varepsilon_s^2 m_s \end{bmatrix} \right) \begin{bmatrix} \bar{u}_s \\ a_s\bar{\varphi}_s \end{bmatrix} = \begin{bmatrix} 0 \\ 0 \end{bmatrix} \tag{14}$$

with the bar denoting modal amplitudes.

2.2.1 Natural frequencies

The characteristic equation, associated with a vanishing determinant in (14), can be written in non-dimensional form as

$$\xi_0^4 - 2\nu_s^2\xi_0^2 + 1 = 0 \tag{15}$$

where the non-dimensional angular frequency ξ_0 is defined as

$$\xi_0^2 = \omega^2 \frac{\sqrt{n_s m_s}}{k_s} = \left(\frac{\omega}{\Omega_s} \right)^2 \tag{16}$$

with respect to the reference angular frequency

$$\Omega_s = \sqrt{\frac{k_s}{\sqrt{n_s m_s}}} \tag{17}$$

representing the geometric mean of the uncoupled translational and rotational frequencies. In (15) the single modal parameter

$$\nu_s^2 = \frac{1}{2} \left(\sqrt{\frac{n_s}{m_s}} + (1 + \varepsilon_s^2) \sqrt{\frac{m_s}{n_s}} \right) \geq 1 \tag{18}$$

determines the two real-valued roots as

$$\xi_{0\pm}^2 = \nu_s^2 \pm \sqrt{(\nu_s^2)^2 - 1} \tag{19}$$

thereby explicitly representing their mean value: $\nu_s^2 = \frac{1}{2}(\xi_{0-}^2 + \xi_{0+}^2)$.

For the normalized root ξ_0^2, the effective coupling is fully defined relative to the structural inertia parameters m_s and n_s by the single modal coupling parameter ν_s^2 in (18), which is bounded by unity so that $(\nu_s^2)^2 - 1$ inside the square root of (19) is guaranteed non-negative. Furthermore, the quadratic equation (15) reproduces the results for *double coupling* in [6], with a double root for $\varepsilon_s = 0$ in the limit $\sqrt{n_s/m_s} \to 1$ and otherwise two distinct solutions: $\xi_{0-}^2 < 1 < \xi_{0+}^2$, related by the inverse point condition $\xi_{0-}^2 \xi_{0+}^2 = 1$.

2.2.2 Mode shape ratio

The coupled mode shape is determined by the $\bar{\varphi}_s/\bar{u}_s$-ratio, governed by the eigenvalue problem in (14). From the first row in (14), the normalized mode shape ratio can be written as

$$\frac{\bar{\varphi}_s e_s}{\bar{u}_s} = 1 - \frac{1}{\xi_0^2} \sqrt{\frac{n_s}{m_s}} \tag{20}$$

with substitution of $\xi_0^2 = \xi_{0-}^2$ and ξ_{0+}^2 determining the low- and high-frequency mode shapes, respectively. It can be shown that the low-frequency mode with $\xi_0^2 = \xi_{0-}^2$ has opposite signs for $\bar{u}_s$ and $\bar{\varphi}_s e_s$, while for the high-frequency mode (ξ_{0+}^2) the transverse and rotation components have equal sign.

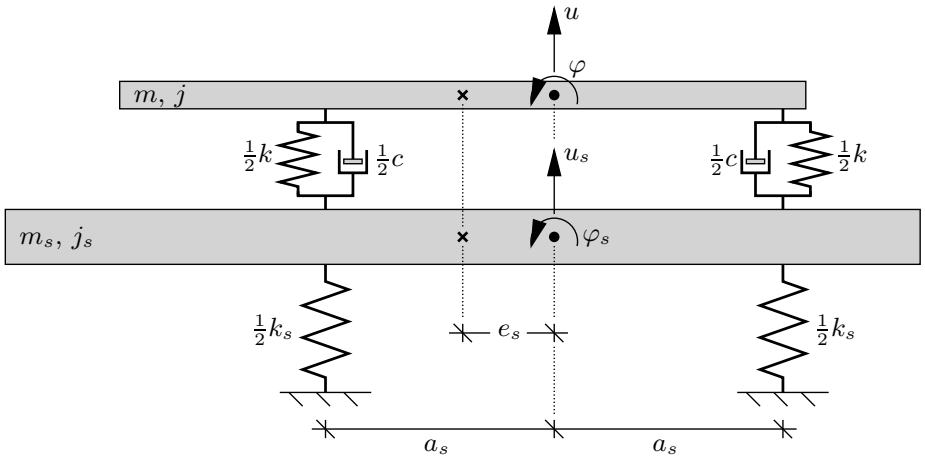

Fig. 4: Coupled two-dof structural model with coupled two-dof tmd. The tmd has analogous coupling properties and is placed with its centers (dot and cross) aligned with those of the structure to secure desired damping performance.

3 Structure model with analogous two-dof tmd

Figure 4 shows the structural model from Fig. 3 with a coupled two-dof tuned mass damped (tmd) governed by its displacement u and rotation φ relative to a common center (dot). The transverse mass of the tmd is m, and its rotational inertia j is defined with respect to the tmd mass midpoint (cross). The tmd mass is suspended to the structure by two pairs of spring-dashpot elements, each with stiffness $\frac{1}{2}k$ and viscous damper coefficient $\frac{1}{2}c$, and separated by distance a_s to the common center (dot). The tmd is placed on the structure so that the centroids (cross) coincide, thereby as well aligning the tmd common center (dot) with the structure shear center (dot). By this analogous tmd configuration, the tmd centroid (cross) is shifted by e_s relative to the common center (dot), at which the corresponding rotational tmd inertia is $J = j + e_s^2 m$. Thus, the present paper considers a coupled two-dof tmd with exactly the same inertia coupling properties as for the structure. It is in the following demonstrated how this analogous principle provides robust tmd performance based on simple design relations.

The analogous principle further implies that the mass ratio for transverse and rotational inertia is the same and in the following represented by a common mass ratio μ. Thus, the two tmd inertial parameters are given as

$$m = \mu m_s \qquad , \qquad j = \mu j_s \tag{21}$$

while $J = \mu J_s$ follows directly from substitution of (21) into $J = j + e_s^2 m$. From these inertia representations, the mass ratio μ is constituted as the fundamental tmd design variable that governs its size and efficiency.

3.1 Reference structure model

The damping in terms of energy dissipation is for the structure-tmd system in Fig. 4 obtained by the dashpots with combined viscous coefficient c. For $c \to 0$ the dashpots disappear and the model in Fig. 4 becomes an undamped four-dof system. The other limit $c \to \infty$ will instead lock the tmd mass rigidly to the structure mass, so that $u = u_s$ and $\varphi = \varphi_s$, assuming coinciding structure and tmd centres. First of all, none of the two limits, $c \to 0$ or ∞, actually recover the original host structure without tmd in Fig. 3 and Section 2.1.3. Instead, a convenient reference frequency is governed by the alternative two-dof system with $c \to \infty$, whereby the tmd inertia is rigidly locked to the structure. In this case, the solutions to the host structure in Section 2.1.3 can be reused, when replacing m_s and n_s by the increased masses $m_s + m$ and $n_s + n$, respectively. Hereby, (16) defines a shifted non-dimensional frequency,

$$\xi^2 = \omega^2 \frac{\sqrt{(n_s + n)(m_s + m)}}{k_s} = (1 + \mu)\left(\frac{\omega}{\Omega_s}\right)^2 = (1 + \mu)\xi_0^2 \tag{22}$$

now without the subscript 0 to distinguish ξ from the pure host structure frequency ξ_0. The analysis of a multi-tmd system for damping of bending-torsion beam vibrations in [47] also uses this shifted reference frequency to obtain closed-form design expressions. Therefore, in the following the calibration obtained from design conditions for the characteristic equation make use of the shifted non-dimensional angular frequency ξ, because the two roots for the

fully combined structure-tmd system will then by construction be inverse points with respect to $\xi = 1$ on the real-valued axis in the complex frequency-plane.

3.2 Coupled structure-tmd equations

As for the host structure model, the coupled equations of motion for the structure-tmd model in Fig. 4 may be established by either energy principles or direct force equilibrium with respect to the governing dofs in the 4×1 displacement vector

$$\mathbf{u}(t) = [\, u_s(t)\,,\ a_s\varphi_s(t)\,, u(t)\,,\ a_s\varphi(t)\,]^T \tag{23}$$

in which rotations are conveniently scaled by a_s. For this structure-tmd system, the governing equations of motion can be written in standard matrix form

$$\mathbf{m}\ddot{\mathbf{u}}(t) + \mathbf{c}\dot{\mathbf{u}}(t) + \mathbf{k}\mathbf{u}(t) = \mathbf{0} \tag{24}$$

introducing the 4×4 mass, damping and stiffness matrices as

$$\mathbf{m} = \begin{bmatrix} \mathbf{m}_s & \mathbf{0} \\ \mathbf{0} & \mu\mathbf{m}_s \end{bmatrix} \quad , \quad \mathbf{c} = c \begin{bmatrix} \mathbf{I}_2 & -\mathbf{I}_2 \\ -\mathbf{I}_2 & \mathbf{I}_2 \end{bmatrix} \quad , \quad \mathbf{k} = k_s \begin{bmatrix} (1+\kappa)\mathbf{I}_2 & -\kappa\mathbf{I}_2 \\ -\kappa\mathbf{I}_2 & \kappa\mathbf{I}_2 \end{bmatrix} \tag{25}$$

with the mass sub-matrix

$$\mathbf{m}_s = m_s \begin{bmatrix} 1 & -\varepsilon_s \\ -\varepsilon_s & n_s/m_s + \varepsilon_s^2 \end{bmatrix} \tag{26}$$

previously used as structural mass matrix in the eigenvalue problem (14) and $\mathbf{I}_2$ denoting the 2×2 identity matrix. In (25) the stiffness matrix $\mathbf{k}$ is conveniently normalized by the structural stiffness k_s, which defines the tmd's stiffness ratio

$$\kappa = \frac{k}{k_s} \tag{27}$$

as a design variable to be calibrated to obtain desirable tmd properties.

3.3 Eigenvalue analysis

As in Section 2.2, the dynamic response is assumed harmonic with angular frequency ω and amplitude $\bar{\mathbf{u}}$. Hereby, the temporal equation (24) is converted into the frequency domain, rendering the quadratic eigenvalue problem

$$\Big(-\omega^2\mathbf{m} + i\omega\mathbf{c} + \mathbf{k}\Big)\bar{\mathbf{u}} = \mathbf{0} \tag{28}$$

with $i = \sqrt{-1}$ being the imaginary unit.

When introducing the 2×2 block matrix form of the mass, stiffness and damping matrices from (25), the associated determinant relation can be expressed as

$$\begin{vmatrix} -\omega^2\mathbf{m}_s + (i\omega c + (1+\kappa)k_s)\mathbf{I}_2 & -(i\omega c + \kappa k_s)\mathbf{I}_2 \\ -(i\omega c + \kappa k_s)\mathbf{I}_2 & -\omega^2\mu\mathbf{m}_s + (i\omega c + (1+\kappa)k_s)\mathbf{I}_2 \end{vmatrix} = 0 \tag{29}$$

Because the applied analogous principle implies that the off-diagonal block components are themselves diagonal, the reduction to the 2×2 determinant relation

$$\Big|\Big(-\omega^2\mathbf{m}_s + (i\omega c + (1+\kappa)k_s)\mathbf{I}_2\Big)\Big(-\omega^2\mu\mathbf{m}_s + (i\omega c + (1+\kappa)k_s)\mathbf{I}_2\Big) - (i\omega c + \kappa k_s)^2\mathbf{I}_2\Big| = 0 \tag{30}$$

follows directly from the recent proof by Silvester [51], which simplifies the derivations because it avoids the use of any matrix inverse.

4 TMD calibration

The characteristic equation obtained from (30) is of 8th polynomial order in the complex natural frequency ω. As argued in Section 3.1, the natural frequency ω is consistently normalized as in (22) to obtain the non-dimensional angular frequency ξ, which secures inverse roots with respect to unity when $c \to \infty$ locks the tmd mass rigidly to the structure.

4.1 The characteristic equation

The characteristic equation is conveniently arranged by collecting all odd-power terms in ξ, as they are all proportional to $i\xi c$, and thus govern the tracing of the root loci in the complex frequency plane between the four real-valued roots for $c \to 0$ and the two real-valued roots (and two roots on the imaginary axis) that are obtained in the other limit $c \to \infty$. All real-valued roots are separately governed by the corresponding even (including zero) power terms in ξ, which are therefore conveniently grouped as well.

Upon extensive use of trivial algebra, the characteristic equation in (30) can be written and organized as

$$\begin{aligned}
&\Big[\big(\xi^2\big)^4 - 2\nu_s^2(1+\mu)\Big(1+\kappa\frac{1+\mu}{\mu}\Big)\big(\xi^2\big)^3 + (1+\mu)^2\Big(1+\kappa^2\frac{(1+\mu)^2}{\mu^2}+2\kappa\frac{\mu+2(\nu_s^2)^2}{\mu}\Big)\big(\xi^2\big)^2 \\
&-2\nu_s^2\kappa\frac{(1+\mu)^3}{\mu}\Big(1+\kappa\frac{1+\mu}{\mu}\Big)\xi^2 + \kappa^2\frac{(1+\mu)^4}{\mu^2}\Big] - \xi^2\eta^2\Big\langle\big(\xi^2\big)^2 - 2\nu_s^2\xi^2 + 1\Big\rangle \\
&-i\xi\eta\Big\{2\nu_s^2\big(\xi^2\big)^3 - 2\Big(\mu+\kappa\frac{(1+\mu)^2}{\mu}+2(\nu_s^2)^2\Big)\big(\xi^2\big)^2 \\
&+2\nu_s^2(1+\mu)\Big(1+2\kappa\frac{1+\mu}{\mu}\Big)\xi^2 - 2\kappa\frac{(1+\mu)^2}{\mu}\Big\} = 0
\end{aligned} \tag{31}$$

when introducing the non-dimensional damper parameter

$$\eta = \frac{c}{\sqrt{k_s\sqrt{n_s m_s}}}\sqrt{\frac{(1+\mu)^3}{\mu^2}} \tag{32}$$

In (31) all odd-power terms are assembled inside the curly braces $\{\dots\}$ with $i\xi\eta$ as common factor. The corresponding even power terms are separated into two groups, with the terms proportional to η^2 placed inside angle brackets $\langle\dots\rangle$, while the remaining even power terms are collected within the square brackets $[\dots]$.

In Fig. 5 the closely spaced blue dots represent root loci of the complex roots ξ obtained by solving the 8th order characteristic polynomial (31) for increasing values of the damper parameter from $\eta = 0$ to ∞. The four sub-figures in Fig. 5(a) to (d) represent four different values of the modal coupling parameter ν_s^2, with identical mass ratio $\mu = 0.05$ and the stiffness ratio κ determined by the tuning formula derived in the next Section 4.2.

For $\eta \to 0$ in (31), the even power terms in the angle brackets and the odd power terms from the curly brackets all vanish, whereby the four real-valued roots associated with vanishing tmd damping ($c \to 0$) are governed by the quartic polynomial in ξ^2 inside the square brackets in (31). In Fig. 5 these four roots are represented by circles, subsequently referred to as $\xi_1 < \xi_2 < 1 < \xi_3 < \xi_4$. In the root locus diagram of Fig. 5(b) for $\nu_s^2 = 1.125$, these four real-valued roots ξ_1 to ξ_4 obtained in the undamped limit ($c \to 0$) are specifically identified below the four circle markers.

For a finite value damper parameter $\eta > 0$, the odd-power terms imply complex roots that for increasing η describe the root loci in the complex ξ-plane. As $\eta \to \infty$ the even power terms proportional to η^2 inside the angle brackets will eventually dominate the characteristic equation (31) and govern the two real-valued roots that determine the natural frequencies of the reference two-dof structure model in Section 3.1 with the tmd rigidly attached. In Fig. 5 these terminal reference roots are depicted by squares, in the following referred to as ξ_{12} and ξ_{34}, with $\xi_{12} < 1 < \xi_{34}$. In Fig. 5(b), the two real-valued roots ξ_1 and ξ_4, associated with locking of the tmd to the structure by $c \to \infty$, are as well specifically depicted at the respective square markers.

4.2 Stiffness calibration

Because the non-dimensional frequency ξ is defined in (22) with respect to the reference two-dof structure model in Section 3.1, the two roots ξ_{12} and ξ_{34}, associated with infinite tmd damping ($\eta \to \infty$), are by construction inverse points with respect to $\xi = 1$ on the real ξ-axis, implying the relation: $\xi_{12}\xi_{34} = 1$. Their solution

$$\xi_{12}^2 = \nu_s^2 - \sqrt{(\nu_s^2)^2 - 1} \quad , \quad \xi_{34}^2 = \nu_s^2 + \sqrt{(\nu_s^2)^2 - 1} \tag{33}$$

is similar to that for ξ_0^2 in (19) for the two-dof structure without absorber and with the modal coupling parameter ν_s^2 defined in (18).

The desired root locus diagrams, as illustrated in Fig. 5, have two separate loci, each with an apparent bifurcation point, similar to the root locus obtained for the classic tmd [25]. Therefore, the four real-valued roots ξ_1 to ξ_4, obtained

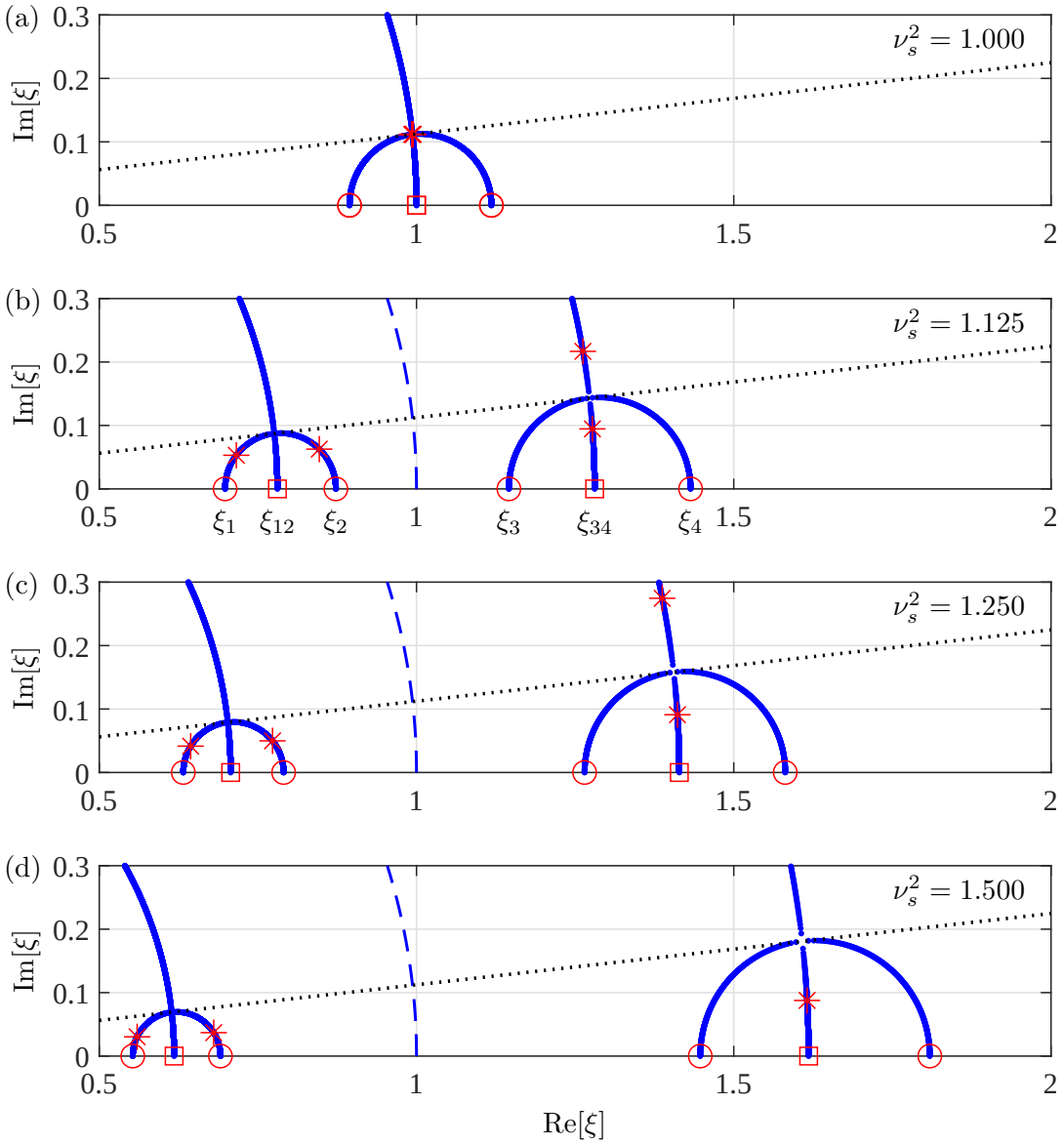

Fig. 5: Root locus diagram for mass ratio $\mu = 0.05$ and modal coupling parameter $\nu_s^2 = 1.000$ (a), 1.125 (b), 1.250 (c) and 1.500 (d), with markers depicting the non-dimensional damping parameters $\eta \to 0$ (four circles), ∞ (two squares) and η_{opt} (four asterisks). In (b) the four and two real-valued roots ξ_1 to ξ_4 and ξ_{12}, ξ_{34}, associated with respectively $\eta \to 0$ and ∞, are depicted below their respective circle and square markers.

by $c \to 0$, must be placed as indicated by the circle markers in Fig. 5 on the real axis, as pairwise inverse points with respect to ξ_{12} and ξ_{34}, whereby $\xi_1\xi_2 = \xi_{12}^2$ and $\xi_3\xi_4 = \xi_{34}^2$. Furthermore, because $\xi_{12}\xi_{34} = 1$ is obtained by construction, the two inverse point conditions directly imply the condition $\xi_1\xi_2\xi_3\xi_4 = 1$. This condition requires that the constant term inside the square bracket in (31) must be unity, which directly determines the desired stiffness ratio as

$$\kappa = \frac{\mu}{(1+\mu)^2} \tag{34}$$

This is the same tuning formula, although expressed for the stiffness ratio and not the isolated tmd frequency, as obtained for the classic tuned mass damper by Den Hartog's fixed-point calibration [23, 25]. By substituting the

stiffness ratio (34) into (31), the characteristic equation can be further reduced to its final form

$$\begin{aligned}\Big[\big(\xi^2\big)^4 - 2\nu_s^2(2+\mu)\big(\xi^2\big)^3 + \Big((1+\mu)(2+\mu)+\mu+(2\nu_s^2)^2\Big)\big(\xi^2\big)^2 - 2\nu_s^2(2+\mu)\xi^2 + 1\Big] \\ -\xi^2\eta^2\Big(\big(\xi^2\big)^2 - 2\nu_s^2\xi^2 + 1\Big) \\ -2i\xi\eta\Big\{\nu_s^2\big(\xi^2\big)^3 - \Big((1+\mu)+2(\nu_s^2)^2\Big)\big(\xi^2\big)^2 + \nu_s^2(3+\mu)\xi^2 - 1\Big\} \;\; = \;\; 0\end{aligned} \tag{35}$$

with the mass ratio μ representing the fundamental tmd design variable, the modal coupling parameter ν_s^2 comprising all structural properties, including the eccentricity ε_s, and damping parameter η constituting the gain parameter in a root locus analysis.

The root loci in Fig. 5 have been produced by sequentially solving the reduced characteristic equation (35) for increasing values of the damper parameter from $\eta = 0$ to ∞. These loci seem to indicate that the outer and inner roots (circles) are respectively pairwise inverse points on the real axis with respect to unity, i.e. $\xi_1\xi_4 = 1$ and $\xi_2\xi_3 = 1$. For the undamped roots associated with $\eta \to 0$ to satisfy both $\xi_1\xi_2 = \xi_{12}^2$ and $\xi_3\xi_4 = \xi_{34}^2$, with as well $\xi_{12}\xi_{34} = 1$, $\xi_1\xi_4 = 1$ and $\xi_2\xi_3 = 1$, the quartic polynomial inside the square brackets in (35) must be identical to a constructed generic 8th order polynomial equation of the form

$$\left(\big(\xi^2\big)^2 - \xi^2\left(\xi_1^2 + \frac{1}{\xi_1^2}\right) + 1\right)\left(\big(\xi^2\big)^2 - \xi^2\left(\frac{\xi_1^2}{\xi_{12}^4} + \frac{\xi_{12}^4}{\xi_1^2}\right) + 1\right) = 0 \tag{36}$$

It is readily found that the terms with $(\xi^2)^3$ and ξ^2 have a common coefficient. Comparison of this common coefficient between (35) and (36) directly determines the root ξ_1^2, and thereby $\xi_2^2 = \xi_{12}^4/\xi_1^2 > \xi_1^2$, as

$$\xi_{1,2}^2 = \frac{\nu_s^2(2+\mu)}{1+\xi_{12}^{-4}}\left(1 \mp \sqrt{1 - \frac{2+\xi_{12}^{-4}+\xi_{12}^4}{(\nu_s^2)^2(2+\mu)^2}}\right) \tag{37}$$

By substitution of ξ_1^2 into (36), its coefficient to the $(\xi^2)^2$-term can now be re-written as

$$2 + \left(\xi_1^2 + \frac{1}{\xi_1^2}\right)\left(\frac{\xi_1^2}{\xi_{12}^4} + \frac{\xi_{12}^4}{\xi_1^2}\right) = 2 + 4(\nu_s^2)^2(2+\mu)^2\frac{1}{(\xi_{34}^2+\xi_{12}^2)^2} + (\xi_{34}^2 - \xi_{12}^2)^2 = 2 + 4\mu + \mu^2 + (2\nu_s^2)^2 \tag{38}$$

with expressions for ξ_{12}^2 and ξ_{34}^2 substituted from (33). The result in (38) is seen to recover the coefficient to the corresponding $(\xi^2)^2$-term in the original characteristic equation (35). Thus, the analogous principle used to construct the coupled two-dof tmd secures all inverse point properties for the damper parameter $\eta \to 0$ when the absorber stiffness ratio is calibrated as in (34).

The applied inverse point conditions furthermore seem to secure the existence of an apparent bifurcation point for each of the two loci in Fig. 5, located along the same (dotted) line with a common damping ratio ζ_* that is independent of the coupling comprised by ν_s^2. The condition for the existence of the bifurcation points is exploited in Appendix A, which shows that they are in fact inverse points with respect to the dashed-blue unit circular curve in Fig. 5. However, the two bifurcation points are not reached for the same value of the damper parameter η, as illustrated in Fig. 5 by the red asterisks, which in (a) to (d) represent the specific value of η that exactly maximizes the smallest damping ratio by a brute force numerical search. For the left ξ_- locus, the asterisks have not reached the bifurcation point yet, while for the right ξ_+ locus they have already passed. Therefore, on the basis of this numerical search the next section derives approximate tuning expressions for the tmd damper parameter η.

4.3 TMD damper optimization

The optimal damper parameter $\eta = \eta_{opt}$ is in the present approach defined as the value that maximizes the smallest of the four damping ratios ζ_{min} from the four complex roots that describe the loci in Fig. 5. For a given complex root ξ, the corresponding damping ratio is defined as its relative imaginary part: $\zeta = \mathrm{Im}[\xi]/|\xi|$. The optimization is simply performed by determining the eight complex roots from (35) for a fixed mass ratio μ and modal coupling parameter ν_s^2, and a damper parameter η varied from 0 to 1.0 with sufficiently small increments. For each damper parameter η the smallest damping ratio ζ_{min} is then identified, whereby η_{opt} is subsequently determined as the specific η-value that maximizes this ζ_{min}, in the following referred to as $\max \zeta_{min}$. As mentioned previously, the asterisks in Fig. 5 represent

the complex roots associated with this optimal damper parameter η_{opt}. For the special case $\nu_s^2 = 1$ in Fig. 5(a), the two structural (and tmd) dofs uncouple, whereby two identical loci, placed exactly on top of each other, are associated with $\max \zeta_{min} = \zeta_* = \frac{1}{2}\sqrt{\mu}$ at the bifurcation point reached by $\eta_{opt} = 2\sqrt{\mu}$, see analysis in Appendix A. For a modal coupling parameter $\nu_s^2 > 1$, approximate tuning expressions for η_{opt} are proposed next.

The solid-line curves in Fig. 6(a) represent η_{opt} as function of the mass ratio μ for $\nu_s^2 = 1.0$ (blue), 1.25 (red), 1.50 (magenta) and 100 (representing ∞ in black). The tendency of the curves in Fig. 6(a) clearly trace a square-root function with respect to μ that decreases in magnitude for increasing values of ν_s^2. The corresponding attainable damping ratio $\max \zeta_{min}$ is shown in Fig. 6(b), exhibiting a substantial reduction in attainable damping (for a given mass ratio) when ν_s^2 increases. Thus, the largest attainable damping is achieved for $\nu_s^2 = 1$, which corresponds to the limit $\varepsilon_s = 0$ and $n_s = m_s$, and the optimal root location at the coinciding bifurcation points in Fig. 5(a). The reduction in attainable damping for $\nu_s^2 > 1$ can be explained by the optimally located asterisks in the root locus diagrams of Fig. 5(b)-(d), for which the distance to the bifurcation point (and its maximum damping ratio $\zeta_* = \frac{1}{2}\sqrt{\mu}$) seemingly increases from (b) to (d), as the modal coupling parameter ν_s^2 becomes larger.

On the basis of the curves in Fig. 6(a), the assumed parametrization

$$\eta_{opt} = g(\nu_s^2)\sqrt{\mu} \tag{39}$$

is used in the optimization to identify an η_{opt}-μ-ν_s^2-dependency, with the assumed damper function $g(\nu_s^2)$ being independent of the mass ratio μ. The embedded optimization function `fminserach` in `Matlab` (Release 2017b) is used to identify g for a given value of ν_s^2 by minimizing its least-squares error between η_{opt} from the previous numerical search procedure and the assumed η_{opt} in (39). The present optimization relies on 100 log-separated data points for ν_s^2 = `logspace(0,2,100)` from 1 to 100. The 100 curves for η_{opt} as function of μ are all plotted in light grey color in the background of Fig. 6(a), with the assumed estimate η_{opt} found by `fminsearch` depicted by circle markers only for the four colored curves, with ν_s^2-values identical to those used for the root locus diagrams in Fig. 5: $\nu_s^2 = 1.0$ (blue), 1.25 (red), 1.50 (magenta) and 100 (black). The colored circle markers in Fig. 6(a) very accurately trace the actual optima (solid-line curves), confirming that (39) captures the optimal absorber damping parameter η with great accuracy across the entire span of ν_s^2 and at least up to a moderate mass ratio of $\mu = 0.1$.

Figure 7 shows the damper function $g(\nu_s^2)$ in blue solid-line for the 100 log-separated ν_s^2-values between 1 and 100. Initially, it is seen that $g = 2$ for $\nu_s^2 = 1$ exactly recovers the analytical solution $\eta_{opt} = 2\sqrt{\mu}$ from Appendix A. In the other limit for $\nu_s^2 \to \infty$ it seems that $g \to \sqrt{2}$. Obtained by ad-hoc curve fitting, the following simple expression

$$g(\nu_s^2) = \sqrt{\frac{4}{(\nu_s^2)^6} - \frac{4}{(\nu_s^2)^4} + \frac{2}{(\nu_s^2)^2} + 2} \tag{40}$$

recovers both desired limits and further captures the steep decline in the damper function g seen in Fig. 7 for smaller values of $\nu_s^2 < 2$. Figure 7 shows this explicit expression (40) as a red dashed-line curve. In Fig. 6(a) the estimate of η_{opt} by (39) with g in (40) is represented by the colored dots, which very accurately reproduce the desired values obtained by the optimized g (circles). Furthermore in Fig. 6(b), the damping ratio (dots) obtained with $\eta = \eta_{opt}$ from (39) and (40) very accurately reproduces $\max \zeta_{min}$ obtained by the numerical search procedure (solid-line).

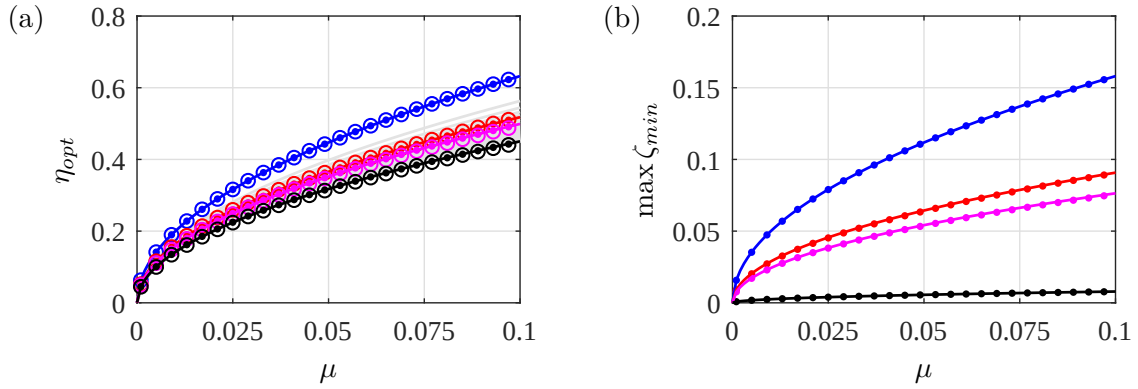

Fig. 6: (a) shows the optimal non-dimensional damping parameter η that for a given mass ratio μ provides the largest minimum damping ratio $\max \zeta_{min}$, shown in (b). The four curves (——) represent a modal coupling parameter $\nu_s^2 = 1.0$ (blue), 1.25 (red), 1.50 (magenta) and 100 (black). The circles represent the optimum curve fit by (39) with the damper function g determined by numerical optimization, while dots represent results for its explicit approximation in (40).

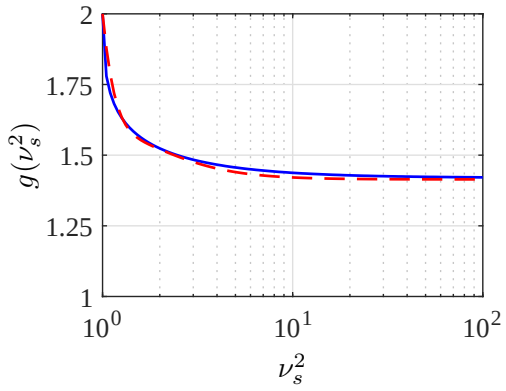

Fig. 7: Identified optimal damper function $g(\nu_s^2)$ (blue solid) as function of modal coupling parameter ν_s^2 by optimum search algorithm, with analytical function (red dashed) in (40) used in the subsequent tmd design.

It is demonstrated in [25] that the maximum damping calibration for a classic tmd, with complex roots placed deliberately at the bifurcation point, is associated with an undesirable increase in dynamic response amplification at resonance, due to constructive interference of the two modes with exactly the same natural frequency. Instead [25] shows, that an optimal reduction in response amplitude is obtained by a viscous damping coefficient that is $1/\sqrt{2}$ times the corresponding coefficient associated with the bifurcation point ($g = 2$ for $\nu_s^2 = 1$). A similar conclusion is obtained in equation (58b) of [52] for piezoelectric shunt damping. In the present case both references [25, 52] therefore suggest that a simple and ν_s^2-independent damper design by

$$g = \frac{2}{\sqrt{2}} = \sqrt{2} \qquad \Rightarrow \qquad \eta_{opt} = \sqrt{2\mu} \tag{41}$$

may be effective with respect to steady-state response mitigation. Furthermore, this design corresponds to the g-limit for large values of ν_s^2 in Fig. 7 and expression (40).

5 Damping of coupled beam vibrations

The efficiency of the coupled two-dof tmd is investigated for a full flexible beam structure with a local tmd attached to target a specific vibration mode $j = s$. The modes $j \neq s$ not targeted by the tmd are associated with two natural frequencies and vibration forms, while the specific mode $j = s$, targeted by the attached tmd, the two associated frequencies split into four with four associated vibration forms. Thus, the total number of natural frequencies (not including complex conjugates) becomes $2N + 2$ for an N-term truncation of the modal expansion (3). The attainable damping for the tmd is in the following assessed both in terms of a root locus analysis in Section 5.3 and a subsequent frequency response analysis in Section 5.4 to investigate its response mitigation properties.

5.1 Beam and tmd properties

The coupled two-dof tmd is attached to the simply supported beam in Fig. 8(a), with a simple (pinned) support with respect to bending and restrained angle of twist at both beam ends. For simplicity the cross-section is assumed cruciform, with dimensions defined previously in Fig. 2. In the following numerical example, the beam properties are chosen as summarized in Table 1, which roughly corresponds to the overall cross-sectional dimensions used to draw the cruciform shapes in Fig. 2(b) and 8(b).

The derivation of the beam cross-section parameters, and the corresponding modal parameters, is conducted in the Appendix B, which for the cross-sectional beam dimensions in Table 1 yield the following modal coupling parameter for mode $s = 1$ and $s = 3$:

$$\nu_1^2 = 1.2553 \qquad , \qquad \nu_3^2 = 2.2221$$

It is noteworthy that for $s = 1$ the actual value $\nu_1^2 = 1.2553$ agrees well with $\nu_s^2 = 1.250$ previously used to obtain the idealized root locus diagram in Fig. 5(c), which thereby constitutes the desired mode 1 result for the root locus analysis conducted for $s = 1$ in Section 5.3.

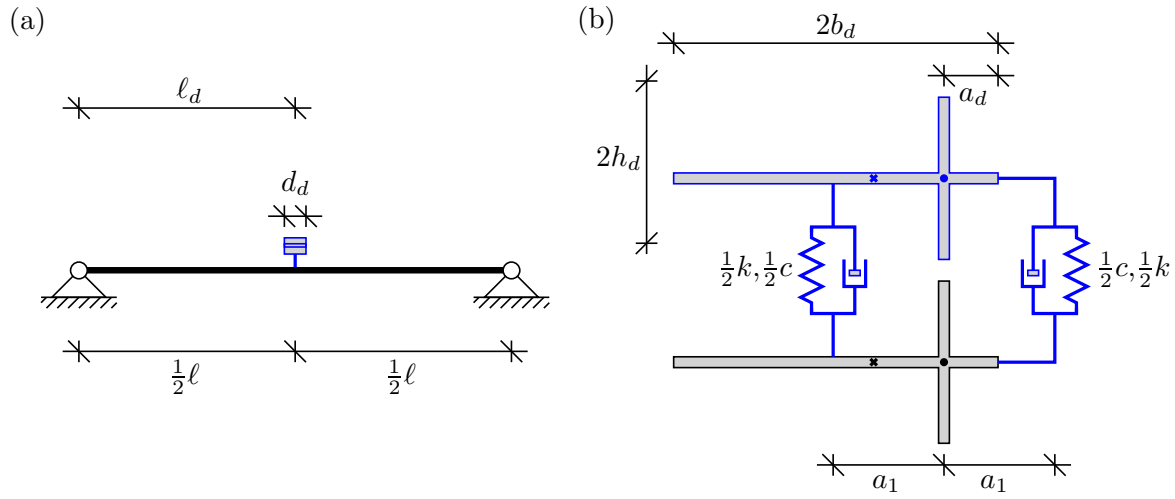

Fig. 8: (a) Simply supported beam with restrained transverse displacement and torsion at both supports and a tmd with depth d_d located at mid span: $\ell_d = \frac{1}{2}\ell$. (b) Analogous cruciform tmd attached to cross-section by spring-dashpot components at distance $\pm a_1$ from shear center (dot).

As depicted in Fig. 8(a), the coupled two-dof tmd is placed at mid-span position $\ell_d = \frac{1}{2}\ell$, with longitudinal depth d_d determining the tmd mass. In Fig. 8(b) the size and shape of the tmd is in the present example assumed identical to that of the corresponding cruciform beam cross-section, whereby the desired analogous properties of the tmd are retained. The coupled two-dof tmd is in the present example calibrated to either the first ($s = 1$) or third ($s = 3$) vibration mode of the beam. Throughout the numerical example, a constant mass ratio is assumed:

$$\mu = 0.05 \qquad \Rightarrow \qquad \kappa = 0.0454 \qquad , \qquad \eta_{opt} = 0.3661 \;\; (0.3162)$$

with the corresponding stiffness ratio κ obtained from (34) and the non-dimensional damping parameter η_{opt} obtained from either (39) and (40) or simply by $\eta_{opt} = \sqrt{2\mu}$ (above value in parenthesis) from (41). The actual tmd parameters are then finally found by

$$m = \mu m_s \qquad , \qquad J = \mu J_s \qquad , \qquad k = \kappa k_s \qquad , \qquad c = \eta \sqrt{k_s \sqrt{n_s m_s}} \sqrt{\frac{\mu^2}{(1+\mu)^3}} \tag{42}$$

with c determined directly from the definition of η in (32).

For the cruciform tmd shape in Fig. 8(b), a set of design equations are derived in Appendix C, which can be used to obtain a desired cruciform geometry that provides the required inertia and coupling properties for the tmd. Cruciform tmd dimensions are in the following depicted by a subscript d for *damper*. Furthermore, the attachment of the tmd by the spring-dashpot components is determined by the modal distance a_s obtained from (B.6) in Appendix B. For modes $s = 1$ and $s = 3$, the corresponding distances are

$$\frac{a_1}{b_d} = 0.684 > 2\frac{a_d}{b_d} \qquad , \qquad \frac{a_3}{b_d} = 0.2279 < \frac{a_d}{b_d}$$

for a given cruciform width dimension $b_d = b$. Thus, when targeting the first mode ($s = 1$), the spring-dashpot element is to one side attached to the beam outside its cross-section (and tmd) boundaries, as indicated in Fig. 8(b) by the additional extensions off the horizontal flanges to the right-side connection points at $z = -a_1$.

Table 1: Beam length and cruciform cross-section dimensions relative to width parameter b.

ℓ/b	a/b	h/b	t/b
30	$\frac{1}{3}$	$\frac{1}{2}$	$\frac{1}{30}$

5.2 Governing modal equations

The fundamental equations are given in (1) and (2) for the beam without tmd. Figure 8(a) shows that the tmd is located at $x = \ell_d$ along the length of the beam, exposing it to a local transverse force $f_d(t)$ and a local torsional moment $t_d(t)$.

5.2.1 Coupled equations with tmd

The tmd forces transferred to the beam are expressed in terms of the spring stiffness k and viscous parameter c as

$$f_d(t) = k\big(u(t) - v(\ell_d,t)\big) + c\big(\dot{u}(t) - \dot{v}(\ell_d,t)\big) \tag{43}$$
$$t_d(t) = ka_s^2\big(\varphi(t) - \theta(\ell_d,t)\big) + ca_s^2\big(\dot{\varphi}(t) - \dot{\theta}(\ell_d,t)\big) \tag{44}$$

and directly included in the beam equations (1) and (2),

$$\rho A\ddot{v}(x,t) - \rho Ae\ddot{\theta}(x,t) + EIv(x,t)'''' - \delta(x-\ell_d)f_d(t) = p(x,t) \tag{45}$$
$$\rho J\ddot{\theta}(x,t) - \rho Ae\ddot{v}(x,t) - GK\theta(x,t)'' - \delta(x-\ell_d)t_d(t) = r(x,t) \tag{46}$$

by a Dirac's delta function $\delta(x-\ell_d)$. The force is correspondingly added (with opposite sign) to the governing ordinary differential equations for the tmd,

$$m\ddot{u}(t) - me\ddot{\varphi}(t) + f_d(t) = 0 \tag{47}$$
$$ma_s^2\left(\frac{n}{m} + \varepsilon_s^2\right)\ddot{\varphi}(t) - me\ddot{u}(t) + t_d(t) = 0 \tag{48}$$

with $m = \mu m_s$ and $n = \mu n_s$ applied in the following.

5.2.2 Modal representation

Sinusoidal expansion functions satisfy the boundary conditions for a simple (pinned) bending support and restrained homogeneous torsion in both of the beam's ends. Thus, the modal representations in (3) are expressed as

$$v(x,t) = \sum_k^N \sin\left(k\pi\frac{x}{\ell}\right)u_k(t) \quad , \quad \theta(x,t) = \sum_k^N \sin\left(k\pi\frac{x}{\ell}\right)\varphi_k(t) \tag{49}$$

with index k truncated at N terms in both expansions. Hereby, these sinusoidal modal expansions correspond to the assumed expansion used in the original paper by Gere and Lin [6].

The modal representations in (49) are substituted into both the two tmd force expressions (43) and (44), and the two governing beam equations (45) and (46). When pre-multiplying the beam equations (45) and (46) with $\sin(j\pi x/\ell)$, then spatially integrating them over the beam length ℓ and finally utilizing (integration by parts and) the orthogonality conditions for sine-functions, a governing set of ordinary differential equations for mode $j = 1, 2, \ldots, N$ can be written as

$$m_j\ddot{u}_j - m_je\ddot{\varphi}_j + k_ju_j - s_jf_d(t) = p_j(t) \tag{50}$$
$$J_j\ddot{\varphi}_j - m_je\ddot{u}_j + k_ja_j^2\varphi_j - s_jt_d(t) = r_j(t) \tag{51}$$

with the short notation

$$s_j = \sin\left(j\pi\frac{\ell_d}{\ell}\right) \tag{52}$$

for the expansion function value at tmd location $x = \ell_d$. The external modal loads are in (50) and (51) defined as

$$p_j(t) = \int_0^\ell p(x,t)\sin\left(j\pi\frac{x}{\ell}\right)dx \quad , \quad r_j(t) = \int_0^\ell r(x,t)\sin\left(j\pi\frac{x}{\ell}\right)dx \tag{53}$$

whereas the local tmd forces in (43) and (44), upon substitution of the modal representations (49), can be expressed as

$$f_d(t) = ku(t) + c\dot{u}(t) - k\sum_k^N s_ku_k(t) - c\sum_k^N s_k\dot{u}_k(t) \tag{54}$$

$$t_d(t) = ka_s^2\varphi(t) + ca_s^2\dot{\varphi}(t) - ka_s^2\sum_k^N s_k\varphi_k(t) - ca_s^2\sum_k^N s_k\dot{\varphi}_k(t) \tag{55}$$

For the chosen mid-span tmd location $\ell_d = \frac{1}{2}\ell$ in Fig. 8(a), all modal deflections s_k with even index k vanish, i.e. $s_2 = s_4 = \cdots = 0$.

5.2.3 Matrix equation

The two tmd force expressions (54) and (55) are now used to eliminate f_d and t_d in (47), (48), (50) and (51), whereby these coupled modal equations can be written in matrix form,

$$\mathbf{M}\ddot{\mathbf{u}}(t) + \mathbf{C}\dot{\mathbf{u}}(t) + \mathbf{K}\mathbf{u}(t) = \mathbf{f}(t) \tag{56}$$

similar to that in (24) for the single mode structure, with the augmented system vector

$$\mathbf{u} = [u_1,\, \varphi_1\,,\;\; u_2,\, \varphi_2\,,\;\ldots\,,\;\; u_N,\, \varphi_N\,,\;\; u,\, \varphi\,]^T \tag{57}$$

now containing $2N + 2$ entries and the corresponding modal load vector

$$\mathbf{f} = [p_1,\, r_1\,,\;\; p_2,\, r_2\,,\;\ldots\,,\;\; p_N,\, r_N\,,\;\; 0,\, 0\,]^T \tag{58}$$

without contributions to the two tmd dofs. The pairwise organization of the modal vectors in (57) and (58) strongly suggests that the same number of terms N is used in both expansions of (49). Thereby, the associated mass matrix will also appear in a block-diagonal form,

$$\mathbf{M} = \begin{bmatrix} m_1 & -m_1 e & & & & & & & & \\ -m_1 e & J_1 & & & & & & & & \\ & & m_2 & -m_2 e & & & & & & \\ & & -m_2 e & J_2 & & & & & & \\ & & & & \ddots & & & & & \\ & & & & & m_N & -m_N e & & & \\ & & & & & -m_N e & J_N & & & \\ & & & & & & & \mu m_s & -\mu m_s e & \\ & & & & & & & -\mu m_s e & \mu J_s & \end{bmatrix} \tag{59}$$

with the bottom block expressed by the common mass ratio μ for the target mode $j = s$. A pure diagonal mass matrix is retained in case of vanishing eccentricity ($e = 0$).

The corresponding stiffness matrix (and damping matrix) impose inter-modal coupling because of the summation terms in the expressions for f_d in (54) and t_d in (55). It is therefore convenient to split the stiffness matrix into

$$\mathbf{K} = \mathbf{K}_m + k\mathbf{B} \tag{60}$$

with a diagonal modal matrix

$$\mathbf{K}_m = \begin{bmatrix} k_1\mathbf{b}_1 & & & & & \\ & k_2\mathbf{b}_2 & & & & \\ & & \ddots & & & \\ & & & k_N\mathbf{b}_N & & \\ & & & & 0\mathbf{b}_s & \end{bmatrix} \tag{61}$$

compactly written in terms of the diagonal 2×2 scaling matrix

$$\mathbf{b}_j = \begin{bmatrix} 1 & 0 \\ 0 & a_j^2 \end{bmatrix} \tag{62}$$

and the, in principle, fully occupied distribution matrix

$$\mathbf{B} = \begin{bmatrix} s_1^2\mathbf{b}_s & s_1 s_2\mathbf{b}_s & \ldots & s_1 s_N\mathbf{b}_s & -s_1\mathbf{b}_s \\ s_2 s_1\mathbf{b}_s & s_2^2\mathbf{b}_s & \ldots & s_2 s_N\mathbf{b}_s & -s_2\mathbf{b}_s \\ \vdots & \vdots & \ddots & \vdots & \vdots \\ s_N s_1\mathbf{b}_s & s_N s_2\mathbf{b}_s & \ldots & s_N^2\mathbf{b}_s & -s_N\mathbf{b}_s \\ -s_1\mathbf{b}_s & -s_2\mathbf{b}_s & \ldots & -s_N\mathbf{b}_s & \mathbf{b}_s \end{bmatrix} \tag{63}$$

that secures the proper influence of the tmd on each of the vibration modes. As the tmd dashpots are located parallel to the springs, the total damping matrix can similarly be written as

$$\mathbf{C} = \mathbf{C}_m + c\mathbf{B} \tag{64}$$

where $\mathbf{C}_m$ is a modal damping matrix, commonly assumed diagonal, comprising all damping sources not attributed to the tmd. Therefore, the following analysis omits $\mathbf{C}_m$ to precisely assess the specific damping performance introduced by the coupled two-dof tmd.

5.3 Root locus analysis

The design and calibration of the coupled two-dof tmd is based on proper placement of the complex poles to maximize the attainable damping in the targeted mode $j = s$, with its two vibration forms denoted by index s_- and s_+. As introduced for the normalized host structure frequencies (ξ_{0-} and ξ_{0+}) in (19), the modal notation (or subscript) j_- and j_+ will in general refer to the two natural frequencies $\omega_{0,j-}$ and $\omega_{0,j+}$ ($> \omega_{0,j-}$) and their corresponding vibration shapes for a specific mode $j = 1, 2, \ldots, N$.

In the previous Fig. 5, for the idealized single-mode structure model, the damping performance is both assessed and calibrated by root loci. In the present section, a root locus analysis is specifically conducted in Section 5.3.2 for the full flexible beam structure with N modes and a coupled two-dof tmd attached.

5.3.1 Undamped vibrations

The dynamic properties of the beam without the tmd are governed by its natural frequencies and associated modes shapes, without approximations determined by respectively (19) and (20) from the analysis of the host structure model. Figure 9 shows the governing parameters for modes $j = 1$ to 10 for the present beam with a cruciform cross-section.

Figure 9(a) presents the governing inertia ratio $\sqrt{n_j/m_j}$, which according to (B.10) increases proportionally with the mode number j (dashed line). The non-dimensional frequencies $\xi_{0,j-}$ and $\xi_{0,j+}$ are pairwise reciprocal values,

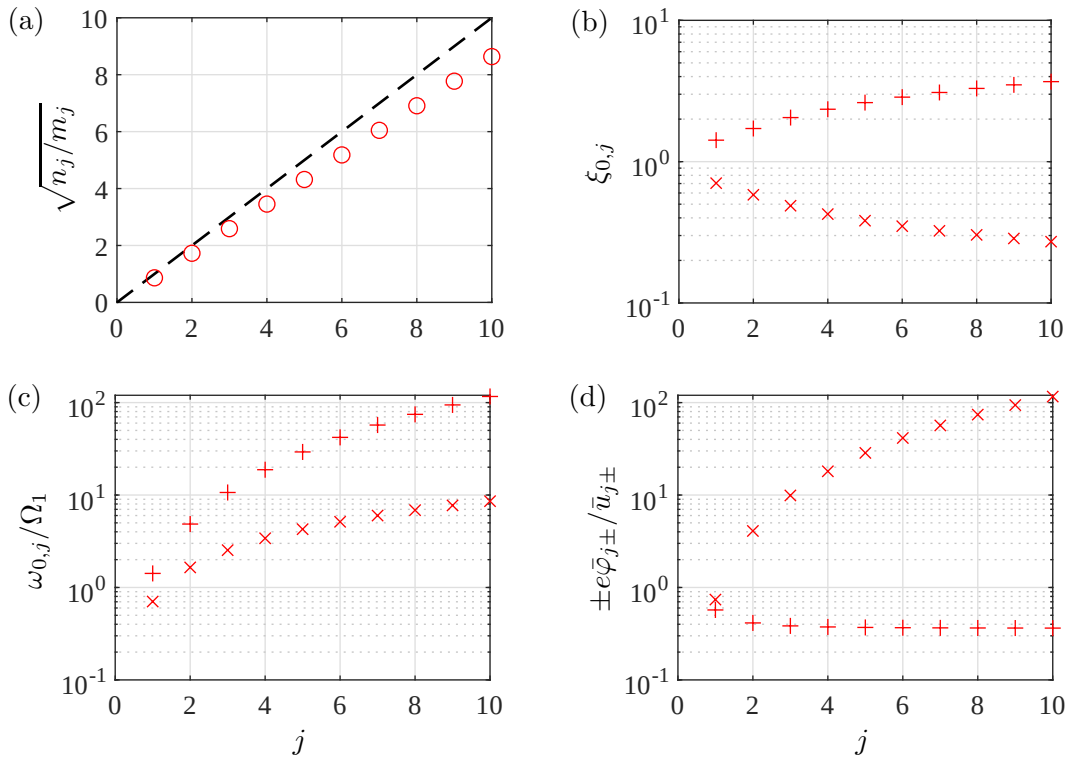

Fig. 9: Plot of host structure properties for modes $j = 1$ to 10: (a) inertia ratio $\sqrt{n_j/m_j}$, (b) normalized modal frequency $\xi_{0,j}$ from (19) with $s = j$, (c) the corresponding frequencies normalized by mode 1 reference frequency $\omega_{0,j}/\Omega_1$ and (d) mode shape displacement ratio at centroid $\bar{\varphi}_j e/\bar{u}_j$. In (b)-(d): smaller frequency (subscript $-$) by crosses and larger (subscript $+$) by plus markers.

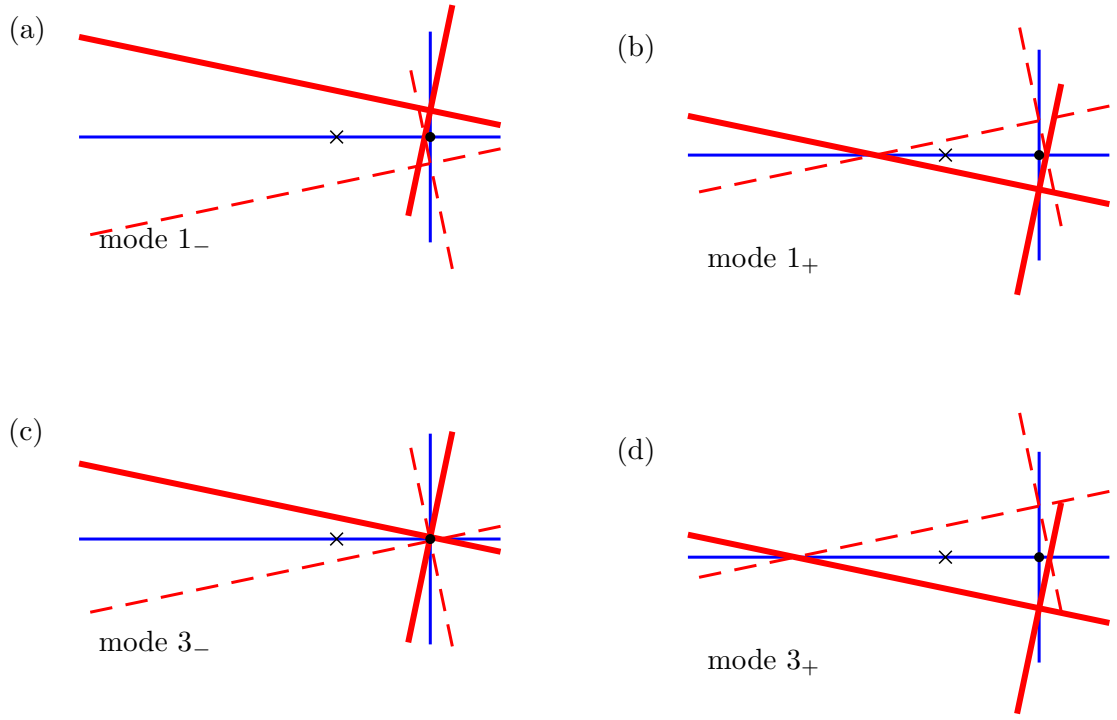

Fig. 10: Plot of relative shape for modes 1_- (a), 1_+ (b), 3_- (c) and 3_+ (d), with centroid (cross) and shear center (dot). Quarter vibration period depicted by sequence: red-solid (extremum), blue-solid (neutral) and red-dashed (opposite extremum).

because $\xi_{0,j-}\xi_{0,j+} = 1$ by construction. Thus, in the semi-logarithmic plot in Fig. 9(b) they are placed symmetrically with respect to $\xi_0 = 10^0$. The corresponding development of the actual natural frequencies $\omega_{0,j\pm}$ as function of j is shown in Fig. 9(c), from which it is seen that e.g. the larger of the mode 3 frequencies is even larger than the smaller of the mode 10 frequencies, i.e. $\omega_{0,3+} > \omega_{0,10-}$. Therefore, the present problem with simultaneous pairwise damping of two coupled vibration forms for a target mode $j = s$ is mostly an issue for the lowest fundamental mode ($s = 1$), with none or only a few frequencies between $\omega_{0,1-}$ and $\omega_{0,1+}$. In the following, a root-locus analysis is thus conducted mainly for the fundamental mode $s = 1$, whereas a higher mode $s = 3$ is merely included to illustrate the ability of the proposed tmd design to specifically target a mode with many other natural frequencies below, between and above $\omega_{0,3-}$ and $\omega_{0,3+}$.

Figure 9(d) shows the mode shape ratio $\bar{\varphi}_j e/\bar{u}_j$, which represents the ratio between the transverse centroid displacement ($\bar{\varphi}_j e$) from the torsion angle and the transverse displacement component ($\bar{u}_j$). The mode shape ratio associated with the lower frequencies (index j_-) is negative, and thus in the logarithmic scale these are plotted by the plus markers with opposite sign. Based on the chosen sign convention in Fig. 3, the mode shapes can be illustrated in terms of in-plane deflections for the cruciform cross-section, as shown in Fig. 10 for the two modes $j = 1$ and 3. The red solid- and dashed-line geometries represent in-plane mode shapes with opposite sign, whereby the sequence from red-solid to blue to red-dashed represent a quarter-period vibration. For modes with non-vanishing torsional component, all in-plane shapes exhibit a zero displacement point where the horizontal flanges of the red-solid and red-dashed geometries intersect. For mode $j = 1_-$ in Fig. 10(a) this neutral point is placed outside to the right of the cross-section boundary, while for the remaining modes (1_+, 3_-, 3_+) in Fig. 10(b-d) they appear along the horizontal flange. The full mode shape with longitudinal dependency may finally be obtained by multiplying either $\bar{u}_j$ and $\bar{\varphi}_j$ or the in-plane shapes in Fig. 10 directly with the common sinusoidal function $\sin(j\pi x/\ell)$ used for the original modal expansion in (49).

When installing the coupled tmd, as shown in Fig. 8, both of the two original target mode frequencies $\omega_{0,s\pm}$ split into two complex frequencies. In case the tmd damping is omitted ($c = 0$), the split frequencies become real-valued, previously denoted in non-dimensional form as ξ_1 to ξ_4 in the analysis of the idealized two-dof model in Section 4 and represented by the circles in the root locus diagrams of Fig. 5. Figure 11 shows the natural frequencies as (blue) dots when a coupled two-dof tmd with mass ratio $\mu = 0.05$ is installed with optimal spring stiffness and without damping. The cross and plus markers are identical to the host structure frequencies from Fig. 9(c). It can be seen that the split frequencies pairwise separate around the undamped frequencies for the target mode $s = 1$ in (a) and $s = 3$ in (b),

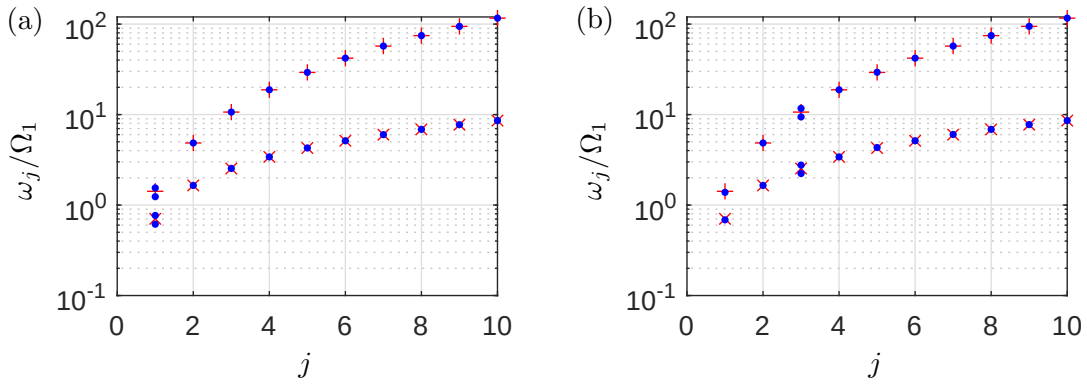

Fig. 11: Plot of normalized structure frequencies ω_j/Ω_1 with undamped tmd ($\mu = 0.05$ and $c = 0$) targeting $s = 1$ (a) and $s = 3$ (b). Host structure solution (19) with $s = j$ shown by cross and plus markers, as in Fig. 9(c).

while leaving the other frequencies ($j \neq s$) virtually unaffected.

5.3.2 Damped vibrations

The performance of the two-dof tmd is now assessed in terms of root locus diagrams, similar to those in Fig. 5 for the pure two-dof structural model. As shown in Fig. 11, the targeted host structure frequencies $\omega_{0,s-}$ and $\omega_{0,s+}$ will each split into two real-valued roots when installing a tmd without damping. For increasing viscous coefficient c, these split frequencies will pairwise trace s_- and s_+ loci in the complex plane.

The complex natural frequencies are determined by the homogeneous form of the equation of motion (56), which in the frequency domain constitutes the eigenvalue problem

$$\big(-\omega^2\mathbf{M} + i\omega\mathbf{C} + \mathbf{K}\big)\bar{\mathbf{u}} = \mathbf{0} \tag{65}$$

with $2N + 2$ complex-valued natural frequencies ω (or their complex conjugates) and corresponding eigenvectors $\bar{\mathbf{u}}$. The eigenvalue problem (65) is conveniently written in state-space form of double size, thereby enabling the use of the `damp`-function in Matlab to determine the $2(2N + 2)$ complex roots (including the complex conjugates) and the associated damping ratios.

Figure 12 shows the root loci for the beam structure with modal truncation at $N = 20$ to secure that all frequencies below and around the largest target frequency (in this case ω_{3+}) are properly accounted for. The closely spaced blue dots describe the loci of the complex frequencies ω for the full flexible beam governed by the eigenvalue problem in

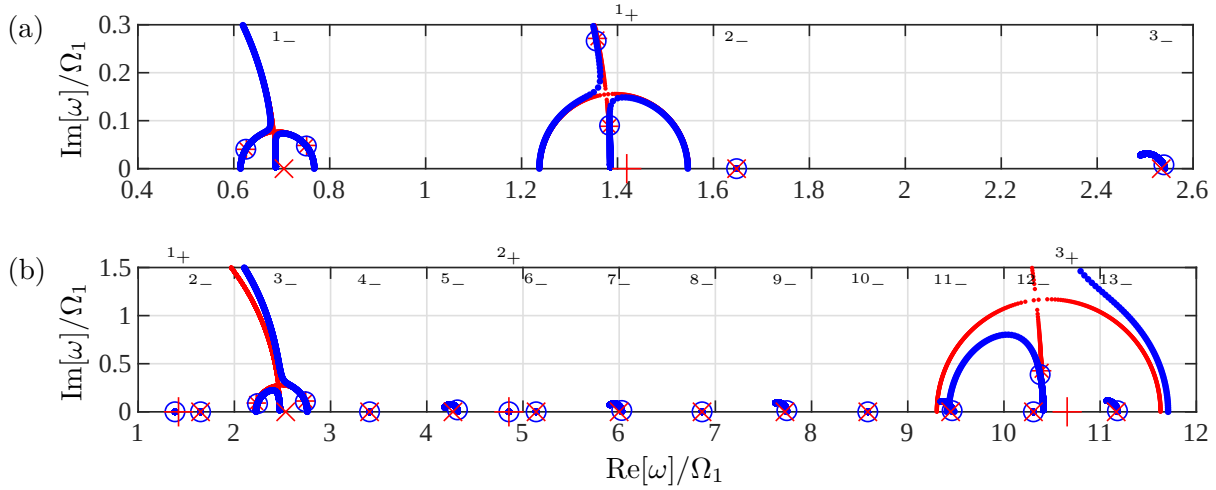

Fig. 12: Root locus diagram for $\mu = 0.05$ and target mode $s = 1$ (a) and $s = 3$ (b). Complex frequencies $\omega_{\pm j}$ are normalized by mode 1 reference frequency Ω_1, while mode numbers $j_\pm$ are written at the top of figures (a) and (b) to depict order of loci.

Table 2: Complex normalized frequencies and damping ratios for target mode $s = 1$ (top) and $s = 3$ (bottom). The mass ratio is $\mu = 0.05$ for both target modes. Damping parameter $\eta = g\sqrt{\mu}$, with g from (40) or $g = \sqrt{2}$ (in parenthesis) from (41).

		$s = 1$		
ω/Ω_1	$0.6250 + i0.0405$	$0.7514 + i0.0472$	$1.3555 + i0.2662$	$1.3834 + i0.0902$
	$(0.6220 + i0.0347)$	$(0.7558 + i0.0410)$	$(1.3540 + i0.1624)$	$(1.3964 + i0.1453)$
ζ	0.0646	0.0627	0.1927	0.0650
	(0.0557)	(0.0541)	(0.1191)	(0.1035)
		$s = 3$		
ω/Ω_1	$2.2402 + i0.0852$	$2.7381 + i0.1050$	$10.128 + i3.3257$	$10.376 + i0.3873$
	$(2.2383 + i0.0799)$	$(2.7405 + i0.0984)$	$(10.2142 + i3.0588)$	$(10.3693 + i0.4203)$
ζ	0.0380	0.0383	0.3120	0.0373
	(0.0357)	(0.0359)	(0.2869)	(0.0405)

(65). The natural frequencies are in the following normalized by the mode 1 reference frequency Ω_1. Figure 12 shows the root locus diagram for target mode $s = 1$ in (a) and $s = 3$ in (b), with mass ratio $\mu = 0.05$ in both cases. The blue circle markers represent the complex frequencies obtained for the tmd damper parameter $c = c_{opt}$ associated with the assumed optimum $\eta_{opt} = 0.3661$ obtained by (39) and (40).

The underlying red dots in Fig. 12 describe the desired optimal root loci obtained by solving the characteristic polynomial (35) with ω subsequently determined by (22). As previously shown in Fig. 5, these optimal loci are inverse root trajectories with respect to $\xi = 1$. For $s = 1$ in Fig. 12(a), the optimal loci are therefore placed inversely with respect to $\mathrm{Re}[\omega]/\Omega_1 = 1/\sqrt{1+\mu} = 0.976$ because the axes in Fig. 12 are normalized by Ω_1. Since $\nu_1^2 = 1.2553 \simeq 1.25$, the placement of the desired (red) loci in Fig. 12(a) are quite similar to that in Fig. 5(c). For target mode $s = 3$, the two optimal (red) loci in Fig. 12(b) are substantially more separated around their inverse point $\mathrm{Re}[\omega]/\Omega_1 = (\Omega_3/\Omega_1)^2/\sqrt{1+\mu} = 5.07$, since $\nu_3^2 = 2.2221 = 1.77\nu_1^2$ is much larger than ν_1^2. The red asterisks in Fig. 12 depict the optimal roots along the optimal (red) loci for the simple two-dof structural model, as also shown in Fig. 5.

In the previous Figs. 9(c) and 11 the red cross and plus markers represent the undamped natural frequencies ($\omega_{0,j-}$ and $\omega_{0,j+}$) of mode j for the host structure without the tmd. These markers are also plotted along the real axis in Fig. 12, with the corresponding mode numbers (j_- and j_+) written at the top of each sub-figure to help identify and order the individual frequencies in the root locus diagrams. For the modes not targeted by the tmd, these host structure frequencies correspond well with the natural frequencies determined by solving the full eigenvalue problem in (65), whereas for the targeted mode they are located slightly to the right of the real-valued terminal roots reached for $c \to \infty$.

For the fundamental mode $s = 1$ as tmd target with $\nu_1^2 = 1.2553$, the pair of root loci (blue dots) in Fig. 12(a) quite accurately reproduce the desired two-dof structure solution (red dots), and the optimum tuning roots (blue circle) also recover the two-dof model predictions (red asterisk). Because the actual root loci are determined for the full flexible beam structure with $N = 20$ modes, the inter-modal coupling imposed by the presence of the tmd results in small deviations, for example seen at the bifurcation points of the underlying red loci, which are not precisely reached by the blue loci for the full flexible beam structure. The frequency range along the real axis in Fig. 12(a) is extended to also include the smaller natural frequencies ω_{2-} and ω_{3-} for the next two modes $j = 2$ and 3, respectively. While mode 2 is unaffected due its nodal point at tmd location, the third mode is seen to receive a small damping contribution because of the modal coupling introduced by the tmd. However, at the desired viscous damping coefficient c_{opt} (blue circle), the higher mode 3_- frequency is virtually undamped because its blue circle marker is placed on the real axis.

For $s = 3$ as target mode with $\nu_3^2 = 2.2221$, Fig. 12(b) clearly shows a much larger number of intermediate modes between and around the loci for ω_{3-} and ω_{3+}. Below the smaller root locus for ω_{3-}, Fig. 12(b) indicates that ω_{1+} is not substantially influenced, while all other odd-numbered modes above (ω_{5-}, ω_{7-} up to ω_{13-}) receive some spill-over damping from the tmd, although for the optimum c (blue circles) the damping in these modes is as well very limited. However, the interaction with other modes implies substantial deviations for the (larger) ω_{3+}-locus, for which the two undamped frequencies (for $c = 0$) are shifted slightly in the high-frequency direction (relative to the underlying red locus), whereas the red and blue loci coincide for $c \to \infty$. This apparent distortion of the (blue) ω_{3+}-locus in Fig. 12(b) explains why the bifurcation condition is so substantially disturbed, resulting in non-optimal damping.

For both target modes $s = 1$ and 3, Table 2 provides the four normalized complex natural frequencies at optimal tuning by (39) and (40), and their corresponding damping ratios. The table values in the parenthesis have instead been obtained for the much simpler damping calibration $\eta = \sqrt{2\mu}$ in (41). In the root locus diagrams of Fig. 12, the complex roots from Table 2 are depicted as blue circles on the target loci. For $s = 3$ in Fig. 12(b) the highly damped root $\omega = (10.128 + i3.3257)\Omega_1$ for mode 3_+ is located on the blue branch outside the figure boundary and therefore not visible. For both target modes, three of the four damping ratios in Table 2 are basically identical, thus almost

exactly reproducing the desired equal modal condition, which in the calibration procedure has been realized by the inverse point conditions. This is even the case for $s = 3$, although in particular the higher ω_{3+}-locus in Fig. 12(b) is strongly distorted by modal interaction. Thus, the proposed calibration method seems to be robust with respect to attainable damping, although improved root locus diagrams could be obtained by for example applying a residual mode correction, as proposed in [30, 47].

When using the simple damper tuning $\eta = \sqrt{2\mu}$ (values in parenthesis in Table 2), the equal damping ratio in the three (of four) complex roots is lost. For $s = 1$ it is seen in Table 2 that by this simple tuning, the two higher complex roots for ω_{1+} are very close and thus located near the bifurcation point, whereas for $s = 3$ this double-pole property is not seen in the bottom table half. However, the simpler design expression $\eta = \sqrt{2\mu}$ is inspired by the tuning of a classical tmd [25], for which it yields improved reduction in frequency response amplitudes, as considered next.

5.4 Frequency response analysis

As shown in Fig. 13 a local force $P(t)$ acts at the beam mid span $x = \frac{1}{2}\ell$ (a), while locally acting on the cross-section in (b) at distance $z = z_p$ relative to the shear center (dot). Thereby, the externally distributed force p and torsional moment r can be introduced to the respective partial differential equations (45) and (46) as

$$p(x,t) = -P\delta(x - \tfrac{1}{2}\ell) \qquad , \qquad r(x,t) = -z_p p(x,t) \tag{66}$$

while the corresponding modal loads are found by substitution into the definitions in (53), which upon evaluation of the integrals give

$$p_j(t) = -\,p(t)\ell\,\frac{1-\cos(j\pi)}{j\pi} \qquad , \qquad r_j(t) = -z_p p_j(t) \tag{67}$$

and thus vanish for all even-numbered modes $j = 2, 4 \ldots$.

The non-homogeneous matrix equation of motion (56) can be expressed in the frequency domain, with assumed harmonic load amplitude $\bar{p}$, thereby introducing a right hand side to (65), which can then be expressed as

$$\big(-\omega^2\mathbf{M} + i\omega\mathbf{C} + \mathbf{K}\big)\bar{\mathbf{u}} = \bar{\mathbf{f}} \tag{68}$$

with the external load vector defined as in (58),

$$\bar{\mathbf{f}} = [\bar{p}_1,\ -z_p\bar{p}_1\ ,\ \ \bar{p}_2,\ -z_p\bar{p}_2\ , \ldots\ ,\ \ \bar{p}_N,\ -z_p\bar{p}_N\ ,\ \ 0,\ 0\ ]^T \tag{69}$$

with the modal moment contributions eliminated by (67b).

Figure 14 shows the frequency response amplitude for the structure and tmd response. The structural response amplitude is assessed in terms of the transverse displacement amplitude

$$\bar{v}_p = \bar{v}(\tfrac{1}{2}\ell) - z_p\bar{\theta}(\tfrac{1}{2}\ell) \tag{70}$$

at the location of the external force ($x = \frac{1}{2}\ell$ and $z = z_p$). The specific blend of transverse displacement and torsional rotation depends on where on the cross-section the transverse displacement is evaluated. For the three values

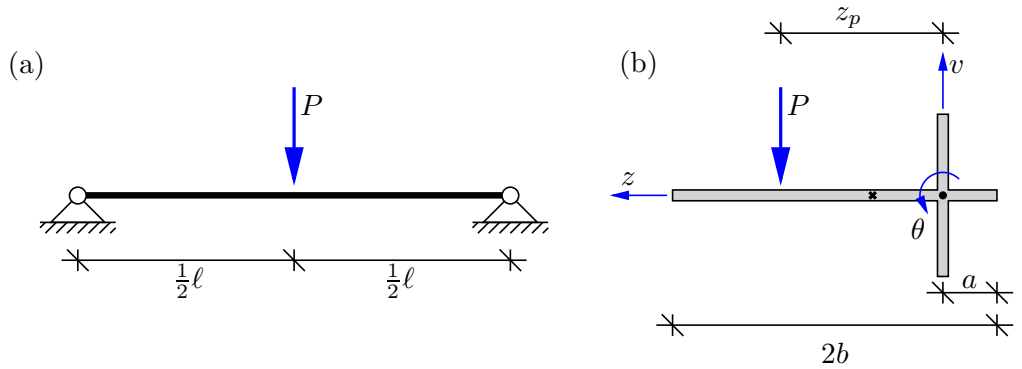

Fig. 13: (a) Simply supported beam with local load P at mid-span, acting vertically on horizontal cross-section flange at horizontal in-plane location $z = z_p$ (b).

$z_p = -a$, 0 and a used in the following, the two mode 1 vibration forms (1_- and 1_+) are in fact excited rather differently and thus the results in Fig. 14 consider various compromises between the two contributions in (70), obtained directly from the frequency domain modal representation of (49),

$$\bar{v}(x) = \sum_j^N \sin\left(j\pi\frac{x}{\ell}\right)\bar{u}_j \qquad , \qquad \bar{\theta}(x) = \sum_j^N \sin\left(j\pi\frac{x}{\ell}\right)\bar{\varphi}_j \tag{71}$$

with the modal components $\bar{u}_j$ and $\bar{\varphi}_j$ contained in the amplitude vector $\bar{\mathbf{u}}$ in (57) found by solving the equation of motion (68). The corresponding tmd amplitudes $\bar{u}$ and $\bar{\varphi}$ are obtained directly from the two last entries in $\bar{\mathbf{u}}$. A representative tmd displacement is in the present example evaluated at the same location as in (70) for the beam cross-section,

$$\bar{u}_p = \bar{u} - z_p\bar{\varphi} \tag{72}$$

with the associated relative tmd displacement $\bar{u}_p - \bar{v}_p$ determining the spring-dashpot elongation.

In Fig. 14 the magnitude (or absolute value) of the complex response amplitude is shown as function of the excitation frequency ω normalized by the mode 1 reference frequency Ω_1. In all sub-figures, both the dynamic structure and tmd amplitudes are normalized by the static structure deflection $\bar{v}_p^0$, obtained by solving (68) in the low-frequency limit ($\omega = 0$). For the frequency response analysis, only $s = 1$ is considered as the tmd target mode, because mode $s = 3$ is both weekly excited by the loading and strongly mitigated by the coupled two-dof tmd. The three left Figs. 14(a,c,e) show the beam frequency response amplitude $|\bar{v}_p|$ for the three different (excitation) locations $z_p = -a$ (a), 0 (c) and a (e), which when normalized by $\bar{v}_p^0$ constitutes the dynamic amplification (or magnification) factor. The corresponding sub-figures (b,d,f) present the frequency amplitude curves for the relative tmd deflection. For both structure and tmd response, the mode 1 response is composed of a left double peak, associated with the lower mode 1_-, and a right single peak, representing the response amplitude at the higher mode 1_+. The blue solid-line curves in Fig. 14 represent the damper tuning obtained by the more elaborate η_{opt} expression in (39) and (40), while the red dashed-line curves represent the simpler formula $\eta_{opt} = \sqrt{2\mu}$ from (41).

Figure 14 shows that the two vibration forms 1_- and 1_+ are excited very differently, depending on the point of loading and/or displacement evaluation (both at $z = z_p$). From the in-plane mode shapes in Fig. 10(a,b), it is seen that at the outermost right position on the cross-section ($z_p = -a$), the transverse displacement is much larger for mode 1_+ in Fig. 10(b) than for mode 1_- in Fig. 10(a), resulting in a frequency response amplitude in Fig. 14(a) clearly dominated by the (right) single-peak resonance at $\omega = \omega_{0,1+} \simeq 1.4\,\Omega_1$. Resonance at this mode 1_+ is only described by a single peak because one of the two vibration forms, represented by $\omega = (1.3555 + i0.2662)\Omega_1$ in Table 2, is so heavily damped, that only the other vibration form with frequency $\omega = (1.3834 + i0.0902)\Omega_1$ is dynamically amplified, with the associated damping ratio somewhat underestimating the actual amplitude ($|\bar{v}_p|/\bar{v}_p^0 \simeq 9$) when using the simple single-dof resonance formula: $1/(2\zeta) = 1/(2 \cdot 0.0650) = 7.7$.

For $z_p = a$, the frequency response is conversely dominated by the mode 1_- resonance in Fig. 14(e,f) because its mode shape in Fig. 10(a) has a much larger deflection at $z = a$ than the corresponding mode 1_+ in Fig. 10(b). The resonance exhibits a well balanced double-peak because the two vibration forms associated with mode 1_- have almost identical damping ratios: $\zeta = 0.0646$ and 0.0627 from Table 2.

For the intermediate case with a forcing and displacement assessment at the shear center ($z_p = 0$), the two mode 1 in-plane vibration shapes (1_- and 1_+) in Fig. 10(a,b) exhibit roughly the same transverse deflection, whereby both the mode 1_- double-peak and the slightly larger mode 1_+ single-peak are visible in Fig. 14(c,d) for the structure and tmd response amplitude.

At all three loading conditions ($z_p = -a$, 0 and a) the coupled two-dof tmd seems to effectively mitigate the vibration amplitude to a dynamic amplification factor below 10 for $\mu = 0.05$. For a classic single-dof tmd on a single-dof structure, the dynamic amplification has been found in [25] to be $\sqrt{(2+\mu)/\mu} = 6.4$. Thus, the present coupled tmd is able to simultaneously provide a level of response mitigation to two coupled modes, which is in the same order of magnitude than that experienced for a pure single-mode problem.

For the double peaks associated with mode 1_- in Fig. 14(c,e), the tmd damping coefficient c could be increased even further to create an even more flat plateau, which would also result in a more flat plateau for the relative tmd response in Fig. 14(d,f). However, an increase in c would conversely reduce the damping in mode 1_+, whereby its single peak would increase. For the simplified tuning with $\eta = \sqrt{2\mu}$, represented by the red dashed curves in Fig. 14, the associated tmd damper coefficient c is in fact reduced slightly compared to the full parametrization in (39) and (40) (blue solid curves). As expected, this reduces the mode 1_+ single peak, at the expense of a marginal increase in the two mode 1_- peaks. Furthermore, the simpler damper tuning $\eta = \sqrt{2\mu}$ results in a slight increase in the mode 1_-

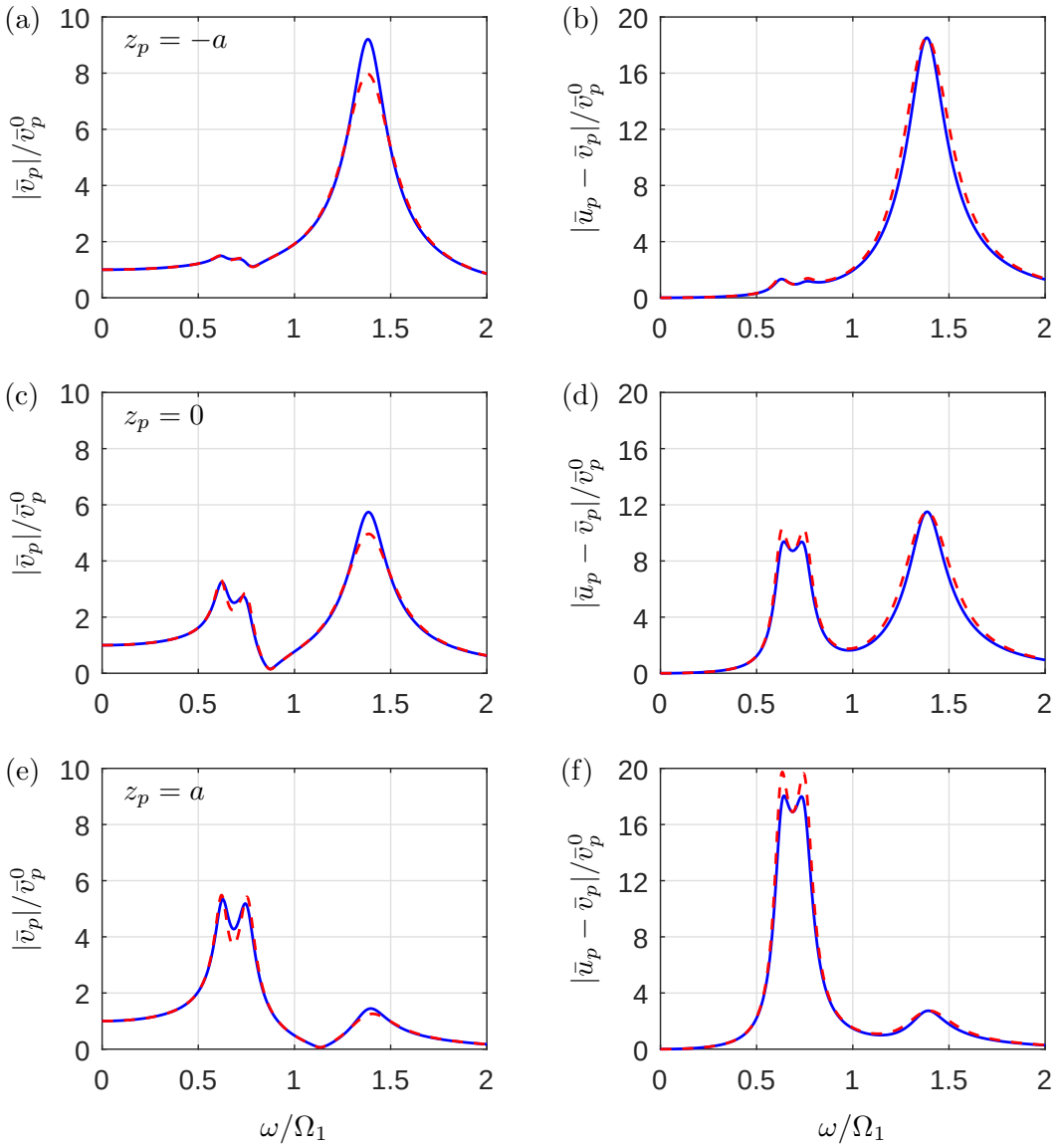

Fig. 14: Frequency response amplitude for beam structure (a,c,e) at $z_p = -a$ (a), 0 (c) and a (e). The relative tmd response is correspondingly shown in (c,d,f). Damping parameter $\eta = g\sqrt{\mu}$, with damper function g from (40) (blue solid) and $g = \sqrt{2}$ (red dashed).

tmd response, see Fig. 14(d,f). However, both tuning expressions for the damper parameter η seem to give fairly good response mitigation, both for the structural deflection in Fig. 14(a,c,e), as well as for the substantially larger (relative) tmd amplitudes in Fig. 14(b,d,f). Thus, because of its much simpler expression, the damper tuning by $\eta_{opt} = \sqrt{2\mu}$ in (41) may be preferred in practice.

6 Conclusions

The present paper concerns the simultaneous damping of the two coupled modes for bending-torsion coupled beam vibrations. By modal decomposition the coupled partial differential beam equations are converted into two coupled ordinary differential equations for the transverse displacement and torsion angle, which together defines a two-degree-of-freedom (two-dof) structure model. The hypothesis of the present paper assumes, that an analogous two-dof tmd, with similar coupling properties, will effectively damp and mitigate the coupled bending-torsion vibrations.

Because of the analogous design of the coupled two-dof tmd, its tuning reduces to the calibration of the spring stiffness and the dashpot viscosity. The former is obtained by requiring the undamped roots associated with vanishing

tmd damping to be pairwise inverse values with respect to the corresponding frequencies obtained by fully locking the tmd to the structure via infinite dashpot viscosity. It is further shown that this stiffness calibration also secures the remaining inverse point conditions to secure two root loci with apparent bifurcation points. Unfortunately, the current tmd configuration implies that the roots do not move along the loci at the same rate, whereby the four complex roots do not reach the bifurcation points for the same damper value. Therefore, in future work the identical dashpots should not be placed in perfect parallel with the springs, thereby introducing an additional design variable that will allow the damping to be scaled in terms of different frequencies ω_{s-} and ω_{s+}.

The theoretical results propose a simple design procedure for coupled two-dof tmd when targetting a coupled bending-torsion vibration mode $j = s$. The procedure initially chooses a common mass ratio μ, which directly determines the stiffness ratio κ by an expression (34) similar to that for the classic single-dof tmd, and the non-dimensional damper parameter η from either the expressions in (39) and (40), which rather accurately secure maximum attainable damping, or by the much simpler expression in (41) that is found to provide sufficient reduction in the frequency response amplitudes. The actual tmd parameters are subsequently obtained by $m = \mu m_s$, $j = \mu j_s$, $k = \kappa k_s$ and c determined from (32), relative to the modal beam properties for the target mode s.

The present vibration problem with a simply supported beam uses sinusoidal expansion functions for both transverse and torsional components, resulting in very accurate tmd performance for the first vibration modes in terms of root locus analysis. For other boundary conditions, for which coupling terms between modes do not necessarily cancel due to orthogonality, the influence from other modes might be more pronounced, leading to a less effective tmd performance than reported in the present example. Furthermore, application to more realistic cases, e.g. involving the vibrations of complex-structured wind turbine blades, and a dedicated comparison with other vibration mitigation measures, which has been found beyond the scope of the present paper, might further illustrate to what extend the proposed simultaneous damping of coupled bending-torsion modes is effective.

Appendix

A Bifurcation point condition

Assume that the complex root $\xi = \xi_* = \mathrm{Re}[\xi_*] + i\mathrm{Im}[\xi_*]$ represents a bifurcation point with both non-negative real and imaginary parts. The inverse point condition with respect to the unit semi-circle determines the other root in the upper-right complex plane as $\xi = 1/\bar{\xi}_*$, with $\bar{\xi}_* = \mathrm{Re}[\xi_*] - i\mathrm{Im}[\xi_*]$ being the complex conjugate of ξ_*. A complex root in the upper-right frequency-plane will have a conjugate root in the neighboring upper-left plane, whereby the remaining two double-roots are $\xi = -\bar{\xi}_*$ and $\xi = -1/\xi_*$. An 8th order polynomial equation, governing the desired two double-roots and their two conjugate counterparts, can thus be constructed as

$$(\xi - \xi_*)^2(\xi - 1/\bar{\xi}_*)^2(\xi + \bar{\xi}_*)^2(\xi + 1/\xi_*)^2 = 0 \tag{A.1}$$

After some use of otherwise straightforward algebra and by collecting terms as in (35), the bifurcation polynomial (A.1) can be expressed as

$$\begin{aligned}\left[\left(\xi^2\right)^4 - 4\chi_*^2\left(\xi^2\right)^3 + 2(1+2\chi_*^4)\left(\xi^2\right)^2 - 4\chi_*^2\xi^2 + 1\right] - \xi^2\Delta_*^2\left\langle\left(\xi^2\right)^2 - 2\xi^2 + 1\right\rangle \\ -2i\Delta_*\xi\left\{\left(\xi^2\right)^3 - (1+2\chi_*^2)\left(\xi^2\right)^2 + (1+2\chi_*^2)\xi^2 - 1\right\} \quad = \quad 0\end{aligned} \tag{A.2}$$

with the governing parameters

$$\chi_*^2 = 1 + 2(|\tilde{\xi}|^2 - 1 + \zeta_*^2) \qquad , \qquad \Delta_* = 4\zeta_*|\tilde{\xi}| \tag{A.3}$$

conveniently defined in terms of a mean absolute root

$$|\tilde{\xi}| = \tfrac{1}{2}\left(|\xi_*| + \frac{1}{|\xi_*|}\right) \tag{A.4}$$

and the common damping ratio

$$\zeta_* = \frac{\mathrm{Im}[\xi_*]}{|\xi_*|} \tag{A.5}$$

representing the dotted lines through the bifurcation points in Fig. 5.

By comparison of (35) and (A.2) it is seen that the even-power terms in the square and angle brackets both satisfy the conditions for the existence of double bifurcation points. However, for the odd-power terms in the curly brackets, the presence of $\nu_s^2 > 1$ disturbs the equivalence, implying that the roots simply do not reach the two bifurcation points for the same value of the damping parameter η.

Only for the special case $\nu_s^2 = 1$ the two coinciding bifurcation points in Fig. 5(a) are reached for the same η. In this case the mean root in (A.4) becomes $|\tilde{\xi}| = 1$, whereby $\chi_*^2 = 1 + 2\zeta_*^2$ and $\Delta_* = 4\zeta_*$ follow from (A.3). Elimination of Δ_* and χ_*^2 in (A.2), followed by comparison with (35), then directly gives $\eta = 2\sqrt{\mu}$ and subsequently $\zeta_* = \frac{1}{2}\sqrt{\mu}$ from (A.5).

B Beam structure properties

B.1 Cross-section parameters

For the cruciform cross-sectional shape in Fig. 2(b), the area A and transverse moment of inertia I with respect to the elastic center (centroid) C are

$$\frac{A}{bt} = 2\left(1 + \frac{h}{b}\right) \quad , \quad \frac{I}{b^3 t} = \frac{2}{3}\left(\frac{h}{b}\right)^3 \tag{B.1}$$

The corresponding mass moment of inertia I_O (with respect to the shear center O) and its torsional stiffness component K are found as

$$\frac{I_O}{b^3 t} = \frac{2}{3}\left(1 + \left(\frac{h}{b}\right)^3\right) + 2\left(1 - \frac{a}{b}\right)^2 \quad , \quad \frac{K}{b^3 t} = \frac{2}{3}\left(\frac{t}{b}\right)^2\left(1 + \frac{h}{b}\right) \tag{B.2}$$

in the following with an elastic modulus ratio $E/G = 2(1 + 0.3)$ assuming isotropic material and a Poisson's ratio of 0.3. The location of the centroid defines the coupling eccentricity, which for the present cruciform cross-section can be determined as

$$\frac{e}{b} = \frac{1 - \frac{a}{b}}{1 + \frac{h}{b}} \tag{B.3}$$

retaining $e = 0$ for $a = b$. The cross-sectional relations in this section can also be used for the assumed cruciform tmd shape in Fig. 8(b) by simply adding the subscript d for *damper*.

B.2 Model parameters

The beam is, as indicated in Fig. 8(a), simply supported in bending and with restrained torsion in both ends. Thus, the expansion functions for mode j are identical and given by pure sines,

$$X_j(x) = Y_j(x) = \sin\left(j\pi\frac{x}{\ell}\right) \tag{B.4}$$

The translation mass and stiffness are then determined by evaluating the integrals in (10),

$$m_j = \tfrac{1}{2}\rho A\ell \quad , \quad k_j = \tfrac{1}{2}(j\pi)^4\frac{EI}{\ell^3} \tag{B.5}$$

while (11) determines the spring-dashpot distance as

$$a_j = \frac{\ell}{j\pi}\sqrt{\frac{GK}{EI}} \tag{B.6}$$

The non-dimensional eccentricity is then determined by (12),

$$\varepsilon_j = \frac{e}{a_j} \tag{B.7}$$

whereby

$$e_j = e \tag{B.8}$$

follows from (8). Finally, the normalized torsional inertia (13) can be written as

$$n_j = \tfrac{1}{2}\rho A\ell\left(\frac{J}{Aa_j^2} - \varepsilon_j^2\right) \tag{B.9}$$

in which the expression inside the parenthesis directly determines the inertia ratio

$$\frac{n_j}{m_j} = \frac{J}{Aa_j^2} - \varepsilon_j^2 = (j\pi)^2\left(\frac{EI}{A\ell^4}\right)\left(\frac{J\ell^2}{GK}\right)\left(1 - \frac{Ae^2}{J}\right) \tag{B.10}$$

that defines the structural modal parameter ν_s^2 in (18).

C Cruciform TMD geometry

For a tmd with cruciform cross-section and length d_d, see Fig. 8, the associated geometry can be chosen to obtain the desired inertia parameters m and J in (42), and the required eccentricity e.

For the tmd parameters (with subscript d) to satisfy the required inertia conditions in (42), the following relations are established

$$\rho_d A_d d_d = \mu m_s \quad , \quad \rho_d I_{O,d} d_d = \mu J_s \quad , \quad e_d = e_s \tag{C.1}$$

with the last relation securing the correct tmd eccentricity. In (C.1) the cruciform area A_d is given by the same expression (B.1a) as for the cruciform beam cross-section, while similarly $I_{O,d}$ is determined by (B.2a) and e_d by (B.3).

The three conditions in (C.1) are interrelated and must therefore be untangled. First, an equation that governs h_d/b_d is determined by eliminating $(1 - a_d/b_d)$ and using $e_s = e$. This yields a cubic polynomial

$$\frac{1}{3}\left(\frac{h_d}{b_d}\right)^3 + \left(\frac{e}{b_d}\right)^2\left(\frac{h_d}{b_d}\right)^2 + \left(2\left(\frac{e}{b_d}\right)^2 - \frac{J_s}{b_d^2 m_s}\right)\left(\frac{h_d}{b_d}\right) + \frac{1}{3} + \left(\frac{e}{b_d}\right)^2 - \frac{J_s}{b_d^2 m_s} = 0 \tag{C.2}$$

that determines the flange height h_d for a given width b_d. The first condition in (C.1), which secures the required translational tmd mass, then determines

$$(\rho_d t_d d_d) b_d = \frac{\frac{1}{2}\mu m_s}{1 + \dfrac{h_d}{b_d}} \tag{C.3}$$

as a single combined parameter, which gives $\rho_d t_d d_d$ for a given value of b_d. Finally, the second condition in (C.1) secures the correct placement of the cruciform intersection at a_d,

$$\frac{a_d}{b_d} = 1 - \sqrt{\frac{\frac{1}{2}\mu J_s}{(\rho_d t_d d_d) b_d} - \frac{1}{3}\left(1 + \left(\frac{h_d}{b_d}\right)^3\right)} \tag{C.4}$$

with substitution of h_d/b_d and $(\rho_d t_d d_d)b_d$ from (C.2) and (C.3), respectively.

In Fig. 8(b) the tmd cruciform dimensions are chosen exactly as those for the beam cross-section, whereby $b_d = b$. Hereby, $e/b_d = \frac{4}{9}$ by (B.3) for the cross-section dimensions in Table 1, which yields $h_d = \frac{1}{2}b = h$ as the only non-negative solution to (C.2). The resulting tmd mass parameter is then obtained from (C.3) as $(\rho_d t_d d_d)b_d = \frac{1}{60}m_1$ for $s = 1$, which for $\rho_d t_d = \rho t$ may determine the tmd depth-to-length ratio as half the mass ratio: $d_d/\ell = \frac{1}{2}\mu = 0.025$. Finally, the location of the cruciform intersection $a_d = \frac{1}{3}b_d = \frac{1}{3}b = a$ is found by (C.4). This shows that for $b_d = b$, the above expressions recover a tmd cruciform geometry that is exactly the same as the shape of the underlying cruciform beam cross-section. For non-cruciform beam cross-sections, the equations (C.2) to (C.4) can as well be used, together with some trial-and-error on governing b_d to avoid any non-positive cruciform dimensions.

References

[1] G. D. Acar and B. F. Feeny. Bend-bend-twist vibrations of a wind turbine blade. *Wind Energy*, 21:15–28, 2018. doi:10.1002/we.2141.

[2] G. T. Michaltsos, E. Sarantithou, and D. S. Sophianopoulos. Flexural-torsional vibration of simply supported open cross-section steel beams under moving loads. *Journal of Sound and Vibration*, 280:479–494, 2005. doi:10.1016/j.jsv.2003.12.041.

[3] R. F. Vieira, D. Lisi, and F. B. Virtuoso. Dynamic analysis of bridge girders submitted to an eccentric moving load. *Structural Engineering and Mechanics*, 52:173–203, 2014. doi:10.12989/SEM.2014.52.1.173.

[4] J. R. Banerjee. A simplified method for the free vibration and flutter analysis of bridge decks. *Journal of Sound and Vibration*, 260:829–845, 2003. doi:10.1016/S0022-460X(02)00929-X.

[5] V. Phung, A. T. Nguyen, H. M. Dang, T. P. Dao, and V. N. Duc. Flexural-torsional vibration of thin-walled beams subjected to combined initial axial load and end bending moment: Application to the design of saw tooth blades. *Shock and Vibration*, 4509630:11pp, 2019. doi:10.1155/2019/4509630.

[6] J. M. Gere and Y. K. Lin. Coupled vibrations of thin-walled beams of open cross-section. *Journal of Applied Mechanics*, 25: 373–378, 1958.

[7] P. Friberg. Coupled vibrations of beams - an exact dynamic element stiffness matrix. *International Journal for Numerical Methods in Engineering*, 19:479–493, 1983. doi:10.1002/nme.1620190403.

[8] E. Dokumaci. An exact solution for coupled bending and torsion vibrations of uniform beams having single cross-sectional symmetry. *Journal of Sound and Vibration*, 119:443–449, 1987. doi:10.1016/0022-460X(87)90408-1.

[9] J. R. Banerjee. Coupled bending torsional dynamic stiffness matrix for beam elements. *International Journal for Numerical Methods in Engineering*, 28:1283–1298, 1989. doi:10.1002/nme.1620280605.

[10] R. E. D. Bishop, S. M. Cannon, and S. Miao. On coupled bending and torsional vibration of uniform beams. *Journal of Sound and Vibration*, 131:457–464, 1989. doi:10.1016/0022-460X(89)91005-5.

[11] J. R. Banerjee and F. W. Williams. Coupled bending-torsional dynamic stiffness matrix for Timoshenko beam elements. *Computers and Structures*, 42:301–310, 1992. doi:10.1016/0045-7949(92)90026-V.

[12] R. D. Ambrosini, J. D. Riera, and R. F. Danesi. A modified Vlasov theory for dynamic analysis of thin-walled and variable open section beams. *Engineering Structures*, 22:890–900, 2000. doi:10.1016/S0141-0296(99)00043-7.

[13] A. N. Bercin and M. Tanaka. Coupled flexural-torsional vibrations of Timoshenko beams. *Journal of Sound and Vibration*, 131: 457–464, 1997. doi:10.1016/0022-460X(89)91005-5.

[14] A. Arpaci and E. Bozdag. On free vibration analysis of thin-walled beams with nonsymmetrical open cross-sections. *Computers and Structures*, 80:691–695, 2002. doi:10.1016/S0045-7949(02)00025-1.

[15] A. Arpaci, E. Bozdag, and E. Sunbuloglu. Triply coupled vibrations of thin-walled open cross-section beams including rotary inertia effects. *Journal of Sound and Vibration*, 260:889–900, 2003. doi:10.1016/S0022-460X(02)00935-5.

[16] D. Ambrosini. On free vibration of nonsymmetrical thin-walled beams. *Thin-Walled Structures*, 47:629–636, 2009. doi:10.1016/j.tws.2008.11.003.

[17] B. Rafezy and W. P. Howson. Exact natural frequencies of a three-dimensional shear-torsion beam with doubly asymmetric cross-section using a two-dimensional approach. *Journal of Sound and Vibration*, 295:1044–1059, 2006. doi:10.1016/j.jsv.2006.02.007.

[18] S. T. Dennis and K. W. Jones. Flexural-torsional vibration of a tapered C-section beam. *Journal of Sound and Vibration*, 393: 401–414, 2017. doi:10.1016/j.jsv.2017.01.017.

[19] J. W. Zhou, S. R. Wen, F. M. Li, and Y. Zhu. Coupled bending and torsional vibrations of non-uniform thin-walled beams by the transfer differential transform method and experiments. *Thin-Walled Structures*, 127:373–388, 2018. doi:10.1016/j.tws.2018.02.026.

[20] C. Mei. Coupled vibrations of thin-walled beams of open section using finite element method. *International Journal of Mechanical Sciences*, 12:883–891, 1970. doi:10.1016/0020-7403(70)90025-1.

[21] M. Tanaka and A. N. Bercin. Finite element modelling of the coupled bending and torsional free vibration of uniform beams with an arbitrary cross-section. *Applied Mathematical Modelling*, 21:339–344, 1997. doi:10.1016/S0307-904X(97)00030-9.

[22] J. E. Brock. A note on the damped vibration absorber. *Journal of Applied Mechanics - Transactions of the ASME*, 13:284, 1946.

[23] J. P. Den Hartog. *Mechanical Vibrations*. Dover, New York, 4th edition, 1985. ISBN 0486647854.

[24] G. B. Warburton. Optimum absorber parameters for various combinations of response and excitation parameters. *Earthquake Engineering and Structural Dynamics*, 10:381–401, 1982. doi:10.1002/eqe.4290100304.

[25] S. Krenk. Frequency analysis of the tuned mass damper. *Journal of Applied Mechanics - Transactions of the ASME*, 72: 936–942, 2005. doi:10.1115/1.2062867.

[26] T. Asami, O. Nishihari, and A. M. Baz. Analytical solutions to H-infinity and H-2 optimization of dynamic vibration absorbers attached to damped linear systems. *Journal of Vibration and Acoustics - Transactions of the ASME*, 124:284–295, 2002. doi:10.1115/1.1456458.

[27] I. F. Lazar, S. A. Neild, and D. J. Wagg. Using an inerter-based device for structural vibration suppression. *Earthquake Engineering and Structural Dynamics*, 43:1129–1147, 2014. doi:10.1002/eqe.2390.

[28] L. Marian and A. Giaralis. Optimal design of a novel tuned mass-damper–inerter (TMDI) passive vibration control configuration for stochastically support-excited structural systems. *Probabilistic Engineering Mechanics*, 38:156–164, 2014. doi:10.1016/j.probengmech.2014.03.007.

[29] D. De Dominico and G. Ricciardi. An enhanced base isolation system equipped with optimal tuned mass damper inerter (TMDI). *Earthquake Engineering and Structural Dynamics*, 47:1169–1192, 2018. doi:10.1002/eqe.3011.

[30] S. Krenk and J. Høgsberg. Tuned resonant mass or inerter-based absorbers: unified calibration with quasi-dynamic flexibility and inertia correction. *Proceedings of the Royal Society A - Mathematical, Physical and Engineering Sciences*, 472:20150718 (23pp), 2016. doi:10.1098/rspa.2015.0718.

[31] S. Elias and V. Matsagar. Research developments in vibration control of structures using passive tuned mass dampers. *Annual Reviews in Control*, 44:129–156, 2017. doi:10.1016/j.arcontrol.2017.09.015.

[32] W. S. Ma, Y. Q. Yang, and J. J. Yu. General routine of suppressing single vibration mode by multi-DOF tuned mass damper: Application of three-DOF. *Mechanical Systems and Signal Processing*, 121:77–96, 2019. doi:10.1016/j.ymssp.2018.11.010.

[33] M. M. A. da Costa, D. A. Castello, C. Magluta, and N. Roitman. On the optimal design and robustness of spatially distributed tuned mass dampers. *Mechanical Systems and Signal Processing*, 150:107289 (25pp), 2021. doi:10.1016/j.ymssp.2020.107289.

[34] H. Garrido, O. Curadelli, and D. Ambrosini. Improvement of tuned mass damper by using rotational inertia through tuned viscous mass damper. *Engineering Structures*, 56:2149–2153, 2013. doi:10.1016/j.engstruct.2013.08.044.

[35] E. Barredo, A. Blanco, J. Colin, V. M. Penagos, A. Abundez, et al. Closed-form solutions for the optimal design of inerter-based dynamic vibration absorbers. *International Journal of Mechanical Sciences*, 144:41–53, 2018. doi:10.1016/j.ijmecsci.2018.05.025.

[36] A. Javidialesaadia and N. E. Wierschem. Optimal design of rotational inertial double tuned mass dampers under random excitation. *Engineering Structures*, 165:412–421, 2018. doi:10.1016/j.engstruct.2018.03.033.

[37] J. M. Renno, M. F. Daqaq, and D. J. Inman. On the optimal energy harvesting from a vibration source. *Journal of Sound and Vibration*, 320:386–405, 2009. doi:10.1016/j.jsv.2008.07.029.

[38] J. C. Snowdon, A. A. Wolfe, and R. L. Kerlin. The cruciform dynamic vibration absorber. *Journal of the Acoustical Society of America*, 75:1792–1799, 1984. doi:10.1121/1.390980.

[39] S. J. Jang and Y. J. Choi. Geometrical design method of multi-degree-of-freedom dynamic vibration absorbers. *Journal of Sound and Vibration*, 303:343–356, 2007. doi:10.1016/j.jsv.2007.01.017.

[40] F. H. Meng, J. C. Wan, Y. J. Xia, Y. Ma, and J. J. Yu. A multi-degree of freedom tuned mass damper design for vibration mitigation of a suspension bridge. *Applied Sciences-Basel*, 10:457 (21pp), 2020. doi:10.3390/app10020457.

[41] J. Høgsberg. Vibration control by piezoelectric proof-mass absorber with resistive-inductive shunt. *Mechanics of Advanced Materials and Structures*, online:(13 pp), 2021. doi:10.1080/15376494.2018.1551587.

[42] M. Berardengo, J. Høgsberg, S. Manzoni, M. Vanali, A. Brandt, et al. LRLC-shunted piezoelectric vibration absorber. *Journal of Sound and Vibration*, 474:115268 (19pp), 2020. doi:10.1016/j.jsv.2020.115268.

[43] L. Zuo and S. A. Nayfeh. The two-degree-of-freedom tuned-mass damper for suppression of single-mode vibration under random and harmonic excitation. *Journal of Vibration and Acoustics - Transactions of the ASME*, 128:56–65, 2006. doi:10.1115/1.2128639.

[44] S. J. Jang, M. J. Brennan, E. Rustighi, and H. J. Jung. A simple method for choosing the parameters of a two degree-of-freedom tuned vibration absorber. *Journal of Sound and Vibration*, 331:4658–4667, 2012. doi:10.1016/j.jsv.2012.05.020.

[45] Y. Q. Yang, W. Dai, and Q. Liu. Design and implementation of two-degree-of-freedom tuned mass damper in milling vibration mitigation. *Journal of Sound and Vibration*, 335:78–88, 2015. doi:10.1016/j.jsv.2014.09.032.

[46] E. Barredo, J. G. M. Larios, J. Mayen, A. A. Flores-Hernandez, J. Colin, et al. Optimal design for high-performance passive dynamic vibration absorbers under random vibration. *Engineering Structures*, 195:469–489, 2019. doi:10.1016/j.engstruct.2019.05.105.

[47] D. Hoffmeyer and J. Høgsberg. Calibration and balancing of multiple tuned mass absorbers for damping of coupled bending-torsion beam vibrations. *Journal of Vibration and Acoustics - Transactions of the ASME*, 142:044501 (8pp), 2020. doi:10.1115/1.4046752.

[48] S. Krenk and J. Høgsberg. Equal modal damping design for a family of resonant vibration control formats. *Journal of Vibration and Control*, 19:1294–1315, 2013. doi:10.1177/1077546312446796.

[49] G. Raze, A. Jadoul, S. Guichaux, V. Broun, and G. Kerschen. A digital nonlinear piezoelectric tuned vibration absorber. *Smart Materials and Structures*, 29:015007 (11pp), 2020. doi:10.1088/1361-665X/ab5176.

[50] R. Darleux, B. Lossouarn, and J. F. Deü. Broadband vibration damping of nonperiodic plates by piezoelectric coupling to their electrical analogues. *Smart Materials and Structures*, 29:054001 (16pp), 2020. doi:10.1088/1361-665X/ab7948.

[51] J. R. Silvester. Determinants of block matrices. *The Mathematical Gazette*, 84:460–467, 2000. doi:10.2307/3620776.

[52] N. W. Hagood and A. von Flotow. Damping of structural vibrations with piezoelectric materials and passive electrical networks. *Journal of Sound and Vibration*, 146:243–268, 1991. doi:10.1016/0022-460X(91)90762-9.